FAILURE ANALYSIS OF STEEL SPECIMENS SUBJECTED TO BLAST LOADS

by

John M. Barsom
and
James V. Pellegrino Jr.

January 30, 2005

Prepared for

American Institute of Steel Construction
One East Wacker Drive, Suite 3100
Chicago, IL 60601-2000

Barsom Consulting Ltd.
1316 Murray Avenue, Suite 300
Pittsburgh, PA 15217
(412) 521-5330

00002

FAILURE ANALYSIS OF STEEL SPECIMENS SUBJECTED TO BLAST LOADS

by

John M. Barsom
and
James V. Pellegrino Jr.

INTRODUCTION

The vulnerability of multi-story steel buildings to disproportionate collapse caused by a terrorist attack and the resilience and capacity of typical steel frame buildings that have been damaged from a blast loading have not been investigated adequately. Large DOD sponsored programs are underway to gather response data on the global behavior of existing steel sections and connections. In support of this effort, the American Institute of Steel Construction (AISC) funded the present companion program to:

1. conduct metallographic and fractographic analyses to identify locations of fracture initiation and fractographic features of fracture initiation and propagation in small blast tested steel specimens.
2. characterize the tensile mechanical properties and notch toughness of the base metal (BM), weld metal (WM) and heat affected zone (HAZ) of the test specimens and their effect on fracture performance of the tested specimens.
3. document the fracture behavior of small test specimens so that, in combination with test results from the DOD programs, their use to predict the behavior of full size steel frame sections and connections may be determined.

BLAST TESTS

Nine 12-inch long specimens of A572 Grade 50 steel were blast tested by the Defense Threat Reduction Agency (DTRA) at Kirkland Air Force Base (KAFB) under the supervision of Karazogian and Case (K&C). Three specimens were rolled W14x132 structural shapes cut next to each other from a single piece. The other six specimens were welded shapes similar in geometry to the rolled sections. They were fabricated of three A572 Grade 50 plates welded using complete penetration welds. The flange plates were 1-inch thick and 14-inches wide, Figure 1. Three specimens were welded with E70T-4 electrode. The remaining three were welded with E70T-6 electrode. The three specimens in each set were blast tested with 10 pounds of C-4 charge. The standoff distances of the charge for the rolled sections were 18, 24, and 30-inch. The standoff distances of the charge for the welded shapes were 24, 30 and 42-inch. The results of the blast tests are presented in Reference 1.

AS RECEIVED SPECIMENS

Pieces about 18 inch long of the W14x132 structural shape and of the A572 Grade 50 built up members welded with E70T-4 and E70T-6 electrodes were shipped to Barsom Consulting, Ltd. The pieces were cut from the same sections that were blast tested. The as fabricated pieces were used to characterize the tensile mechanical properties and the notch toughness of the BMs, WMs, and HAZs.

The tested specimens were shipped to Barsom Consulting, Ltd., Figure 2. In general, the specimens fractured at the web-to-flange joints. Consequently, one of the web/flange fractures for each specimen was arbitrarily designated as Fracture A, the other Fracture B. Figure 3 presents an example of this marking for web/flange fracture in Specimen 2. Subsequently, the location(s) of fracture initiation for every web/flange fracture was identified and marked as shown in Figure 4 for the web of Specimen 4 and in Figure 5 for Flange A of Specimen 5. General views of the tested specimens, their fractures and the marks identifying fracture origins are presented in Appendix A.

MACRO IMAGES OF FRACTURE INITIATION

Most fracture surfaces of the blast tested specimens were severely corroded/oxidized. Cleaning and stripping the fracture initiation sites and surrounding area were partially successful in removing the adherent corrosion products.

Rolled W-Shape Test Specimens

Specimens 1, 4 and 7 were rolled W14x132 structural shapes tested at charge standoff distances of 24, 16 and 30 inch, respectively. The web and flanges of Specimen 1 deformed severely without breaking, Figure 6. The webs of Specimens 4 and 7 deformed plastically then separated from the flanges. Maximum plastic displacement to fracture of the web in Specimen 4 was larger than in Specimen 7, Figure 6. Fractures of both specimens initiated in the webs along the maximum stress concentration at the web/flange fillets. Figures 7 and 8 are fractographic images of the web at the location of crack initiation along the fillet radius. Visual examination of the fracture surfaces indicated that the fractures in Specimens 4 and 7 initiated and propagated in a ductile shear manner. Crack propagations beyond this depth were different. Crack propagation in Specimen 4 continued to be ductile shear through the web thickness. Crack propagation in Specimen 7 changed to flat brittle appearance at mid-thickness of the web then to primarily ductile shear at termination of the fracture.

Cross sections through the fractures of Specimens 4 and 7 are presented in Figures 9 and 10, respectively. They show that the fracture in Specimen 4 initiated and propagated through the thickness of the web along the 45/60 degree shear planes. The cross section in Figure 10 shows that the fracture in Specimen 7 initiated and propagated about 0.25-inch along a shear plane then about 0.5-inch perpendicular to the applied tension and bending stresses caused by the blast load. Finally, the crack changes to shear slip-plane propagation.

Scanning electron microscopy (SEM) images of the fracture surfaces of Specimens 4 and 7 are presented in Figures 11 and 12, respectively. These microscopic images confirmed the preceding observations. Fracture of Specimen 4 initiated and propagated by ductile shear void coalescence along slip planes. Fracture of Specimen 7 initiated and terminated by ductile shear void coalescence along slip planes. Between the initiation and termination, it propagated in a brittle cleavage manner.

Test Specimens Welded With E70T-4 Electrode

Specimens 2, 5 and 8 were welded with an E70T-4 electrode and tested at charge standoff distances of 24, 30 and 42 inch, respectively. The webs of the specimens were severed from the flanges, Figure 13. The webs were subjected to different plastic deformations prior to fracture. The web at 24-inch standoff distance deformed in the shape of a sine wave. At 30-inch standoff distance the web deformed asymmetrically with maximum plastic deflection at about third width. At 42-inch standoff distance, the web deformed symmetrically with maximum plastic deflection at mid width.

Fractographic images of fracture initiation and propagation for Specimens 2, 5 and 8 are presented in Figures 14, 15 and 16, respectively. The fractures exhibited primarily brittle features. Fractures of Specimens 2 and 8 initiated at the toe of the weld on the flange faces and propagated into the flange producing a divot fracture. Fracture of Fracture A in Specimen 5 initiated on the weld surface between weld passes. Some lack of fusion and porosity were present at about mid thickness of the weld. However, the discontinuities did not contribute to the fracture. Fracture of Fracture B in Specimen 5 initiated in the weld metal at the toe along the web. Close up images of several fracture initiation sites in Specimens 2, 5 and 8 revealed the presence of porosity, Figures 14, 15 and 16, respectively. The fractures appeared to have initiated in a ductile manner for a very short distance that varied between about 0.012 and 0.025 inch.

Cross sections through fracture initiations of Specimens 2, 5 and 8 are presented in Figures 17, 18 and 19, respectively. They demonstrate that the fractures initiated in the weld metal and that flange divot fractures formed when fracture initiated at weld toes along flange faces.

SEM images of the fracture surfaces for Specimens 2, 5 and 8 are presented in Figures 20, 21 and 22, respectively. They demonstrate that fractures initiated ductilely for a very short distance and propagated in a brittle manner.

Test Specimens Welded With E70T-6 Electrode

Specimens 3, 6 and 9 were welded with an E70T-6 electrode and tested at standoff charge distances of 24, 30 and 42 inch, respectively. The web-to-flange welds of Specimens 3 and 6 fractured at both flanges, Figure 20. Only one weld in Specimen 9 fractured. Figure 20 shows that plastic deformation at fracture occurred at about one third width of the web and at mid width in Specimens 6 and 9. Maximum plastic deflections at fracture were about equal in Specimens 3 and 6 and was much larger in Specimen 9 tested at 42 inch charge standoff distance.

Fractographic images of fracture initiation and propagation for Specimens 3, 6 and 9 are presented in Figures 21, 22 and 23, respectively. They indicate that the fracture initiated at the toe of the weld in the web and propagated about 0.2 to o.25 inch in ductile shear. Cross sections through fracture initiation locations in Specimens 3, 6 and 9 are presented in Figures 24, 25 and 26, respectively. They demonstrate that ductile initiation and propagation occurred in the heat affected zone of the web plate. Subsequently, the fracture propagated in a brittle manner and terminated in a ductile manner.

Material Properties

Examination of the blast tested specimens showed that the fractures initiated at stress risers of the web/flange fillet radius for the W14x132 structural shape and at the weld toes for the welded specimens. Because of the short distance from fracture initiation to the outside surface of the flanges, 0.25-inch specimens were machined transverse to the k-line and to the deposited weld metal to ensure that the locations of fracture initiation in the blast tested specimens would be located within the uniformly stresses section of the tensile specimens.

The room temperature tensile properties transverse to the k-line of the W14 x 132 rolled section and transverse to the deposited E70T-4 and E70T-6 weldments are presented in Table 1. Yield and tensile strengths of the rolled section were higher than for the weldments, however, elongation and reduction of area were the same for the three specimen types. Fractures of the E70T-4 tension specimens were in weld metal. The E70T-6 tension specimens fractured in the base metal HAZ. The stress-strain curves for the three types of blast tested specimens are presented in Figures 27, 28 and 29.

Room temperature Charpy V-notch toughness test results of the BM, WM and HAZ are presented in Table 2. The W14x132 rolled section exhibited 10 ft-lb energy absorption and zero shear fracture. The deposited E70T-4 weld metal had an average 13 ft-lb energy absorption and 19 percent shear fracture. The deposited E70T-6 weld metal had an average 47 ft-lb energy absorption and 66 percent shear fracture. The HAZ along the E70T-4 and E70T-6 deposited weld metals had an average 66 ft-lb energy absorption and 63 percent shear fracture, and 38 ft-lb energy absorption and 43 percent shear fracture, respectively.

DISCUSSION

The three types of blast tested specimens resulted in fractures that could not be correlated with tensile mechanical properties or notch toughness. The room temperature transverse tensile specimens across the k-line and the deposited weld metals had equal elongations and reduction of area. Therefore, differences in fracture performance could not be related to these properties.

The A572 Grade 50 W14x132 structural shape Specimen 1 tested at 24 inch charge standoff distances deformed severely and did not fracture. The W14x132 Specimens 4 and 7 tested at 18 and 30 inch standoff distances, respectively, fractured in a ductile manner through the web thickness. The ductile shear fractures initiated in the k-line of the W14x132 sections at the location of maximum stress concentration in the web/flange fillet radius. The notch toughness of the BM at this location was 10 f-lb at 70°F with zero to 5 percent shear fracture. At this level of notch toughness, cracks should propagate in a brittle manner unless fracture toughness is not the governing parameter. The large deformation of Specimen 1 and the ductile shear fractures of Specimens 4 and 7 along slip planes of the W14x132 specimens indicated that the steel shear strength rather than fracture toughness were the controlling parameters. This observation should not be construed to imply that fracture toughness can be discounted as a contributing factor to the fracture performance of steel components subjected to blast loads.

The deposited E70T-4 weld metal had lower strength and very similar elongation, reduction of area and notch toughness as the steel of the W14x132 structural specimens. However, unlike the blast performance of the rolled sections, the specimens welded with E70T-4 electrode initiated and propagated in the weld metal. Initiation occurred at stress risers with a very small ductile zone and propagated through the weld metal in a brittle manner. Fracture toughness of the deposited E70T-4 weld metal was a contributing factor to the brittle crack propagation behavior.

Failure of the A572 Grade 50 specimens welded with E70T-6 electrodes fractured at the stress concentrations along the weld toe in the web. The fractures initiated and propagated about 0.25 inch in a ductile manner in the HAZ. The HAZ had an average impact Charpy V-notch toughness of 30 ft-lb at 70°F, which corresponds to about 68ksi√in impact fracture toughness [2]. The depth of the ductile fracture initiation and propagation zone was constant irrespective of the charge standoff distance and, therefore, the blast pressure. This behavior indicates that the fractures were not governed by fracture toughness. The WM had an average notch toughness of 47 ft-lb at 70°F. The deposited E70T-6 WM had adequate fracture toughness and fracture resistance to prevent WM fracture under the blast test loads.

ANOMALIES

Fractures of the blast tested specimens indicated that the test results were influenced by uncontrolled test parameters. Specimens 1, 4 and 7 were cut adjacent to each other from a single A573 Grade 50 W14x132 rolled section. Negligible variation in chemical composition, processing and mechanical properties would be present within such a small rolled length. Therefore, any differences in deformations were, most likely, related to testing variables. Web maximum plastic deflection at fracture for Specimen 4 at 18-inch charge standoff distance was essentially equal to that of Specimen 7 at 30-inch standoff distance. On the other hand, Specimen 1 at 24-inch standoff distance deformed severely and did not fracture. This contradictory behavior questions the reproducibility of the test.

Maximum plastic deflections of W14x132 Specimens 4 and 7 tested at 18- and 30-inch charge standoff distances, respectively, were essentially equal to the deflections of Specimens 2, 5 and 8 of the E70T-4 welded specimens tested at 24, 30 and 42 inch standoff distance, respectively. This similar behavior occurred despite the significant difference in fracture behavior from fully ductile for the rolled sections to primarily brittle for the welded specimens.

Web plastic deformations to fracture of the specimen welded with E70T-4 electrode are unique, Figure 13. At 24-inch charge standoff distance, the blast load deformed the web of Specimen 2 into a sinusoidal wave. Maximum positive plastic deflections to fracture, in the direction of blast loading, occurred at about one third widths of the web. The web did not deform at midwidth. Web of Specimen 5 tested at 30-inch standoff distance, exhibited asymmetric plastic deformation with maximum deflection to fracture on one side at about third width. At 42-inch standoff distance, the web of Specimen 8 exhibited a symmetric deformation with maximum plastic deflection to fracture at midwidth. These significantly different web deformations cannot be related to differences in steel properties. They must be related to nonuniformity of the blast pressure and differences in the boundary conditions at the welded and bolted "feet" of the test specimens. The welds attaching the feet to flange edges were very different in size, length and strength. Some feet broke off with minimum specimen deformation while others remained attached to the flanges despite severe specimen deformations. The differences in web deformations to fracture may be related, also, to nonuniform fastening of the feet to the concrete base. The different response of the web deformations to the blast charges suggest that cladding may have a significant effect on the performance of steel sections subjected to blast loads.

Pretest analyses were performed by K&C to estimate the size of the charge to be used and to determine an appropriate standoff to produce a response of interest [1]. The analyses were performed using LS-

DYNA [3], a nonlinear finite element analysis program. The blast loads were estimated using ConWep [4], a program used to estimate pressure and impulse based on charge weight and standoff. Dunn [1] states that ConWep "is likely to produce only a rough estimate of the actual loading because of the close standoff and shape of the specimens." Failure analysis of the tested specimens indicates that the blast pressure was excessive and nonuniform. The analytically predicted behavior of the blast tested specimens were significantly different from the actual performance of the specimens [1]. The predictive capabilities of the analyses need to be investigated and improved. Also, the test conditions required to ensure reproducibility of the tests must be established before this type of testing is used to characterize the performance of steel sections under blast loading conditions.

CONCLUSIONS

Fracture analyses have been conducted on blast loaded A572 Grade 50 W14x132 structural shape specimens and similar shapes of A572 Grade 50 plates welded with E70T-4 and E70T-6 electrodes. The following are a few conclusions based in the results of the present investigation.

1. There were no obvious correlations between fracture performance and tensile mechanical properties or notch toughness of the steels or deposited weld metals.

2. Variability of web plastic deformations to fracture indicated that the blast pressures at short and intermediate charge standoff distances were not uniform across the web.

3. Nonuniform deformations of the web suggest that the presence of cladding between the charge and the test specimen could affect the fracture performance significantly.

4. Deformations and fractures of the web and flanges, especially at short charge standoff distances, indicated that the specimens were subjected to stresses that exceeded the ultimate shear and tensile properties of the steel.

5. Variabilities in fixturing and attaching the test specimens to the concrete pedestal appear to have affected the fracture performance.

6. Finite element analysis predicted deformations and fractures significantly different from actual performance of the tested specimens. The differences may be caused either from the finite element analysis or from the model used to predict the desired charge weight and standoff distance.

7. The test conditions required to ensure reproducibility of test results must be established before this type of blast test is used to characterize the performance of steel components under blast conditions.

REFERENCES

1. Dunn, B. W., "AISC Steel Materials Testing – Final Report," Karagozian and Case, January 10, 2005.

2. Barsom, J. M. and Rolfe, S.T., *Fracture and Fatigue Control in Structures – Applications of Fracture Mechanics*, 3rd edition ASTM MNL41, ASTM International, West Conshohocken, 1999.

3. "LS-DYNA User's Manual – Version 960," Livemore Software Technology Corporation, March 2001.

4. Hyde, D. W., "User's Guide for Microcomputer Programs ConWep and FunPro, Applications of TM 5-855-1. 'Fundamentals of Protective Design for Conventional Weapons'," Instruction Report SL-88-1, Department of the Army, Waterways Experimental Station, Corps of Engineers, Vicksburg, MS 1988.

Table 1. Mechanical Properties at 70°F

	Yield Strength ksi	Tensile Strength ksi	Elongation %	Reduction of Area %	Fracture Location
W14x132	88.5	89.0	13	65	BM
	87.5	89.0	16	66	BM
	89.0	90.0	15	63	BM
E70T-4 Weldment	61.0	82.0	13	57	WM
	64.5	82.0	14	59	WM
	65.0	83.5	12	61	WM
E70T-6 Weldment	65.0	84.0	13	67	HAZ
	66.0	81.0	9	65	HAZ
	66.5	83.5	18	66	HAZ

Table 2. Charpy V-Notch Toughness at 70°F

	Location	Absorbed Energy, ft-lb	Lateral Expansion, inch	Shear, %
W14x132	BM	10	0.007	5
		10	0.0065	0
		10	0.005	0
E70T-4	WM	12	0.012	6
		14	0.013	26
		14	0.015	26
E70T-4	HAZ	58	0.027	30
		72	0.059	75
		68	0.055	85
E70T-6	WM	50	0.043	70
		62	0.053	82
		30	0.032	47
E70T-6	HAZ	38	0.035	47
		36	0.033	36
		40	0.038	47

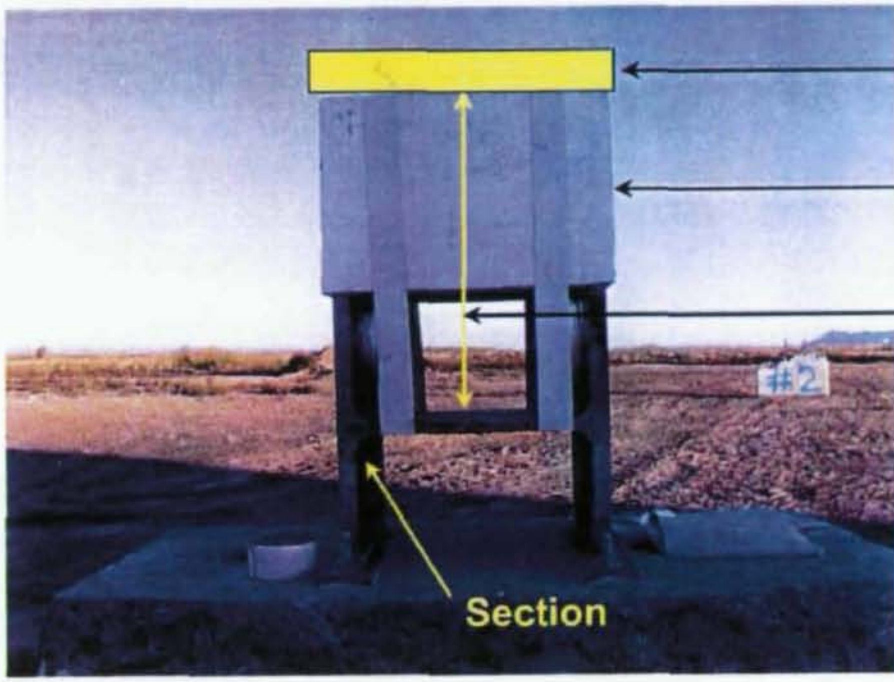

Figure 1.1.

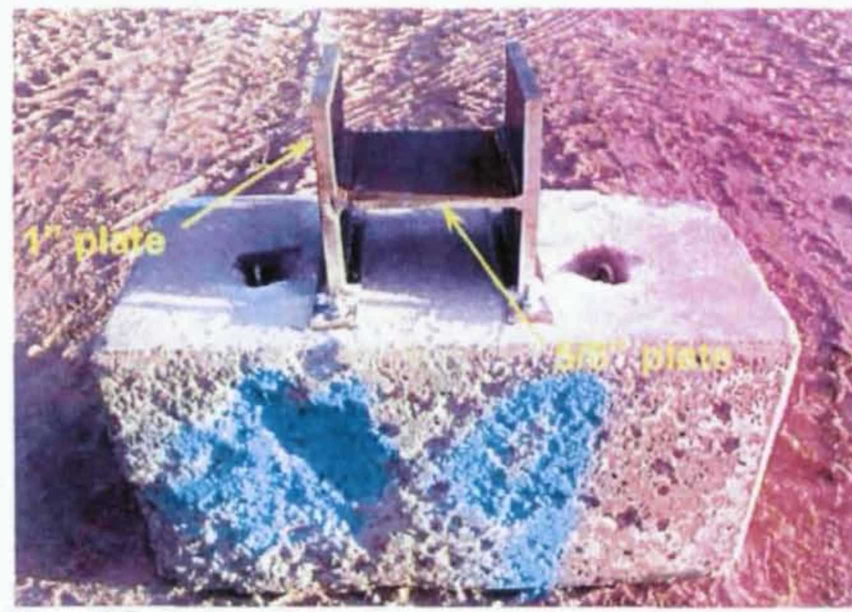

Figure 1.2.

Figure 1. Weld test specimen and test setup[1].

Figure 2. Tested specimens

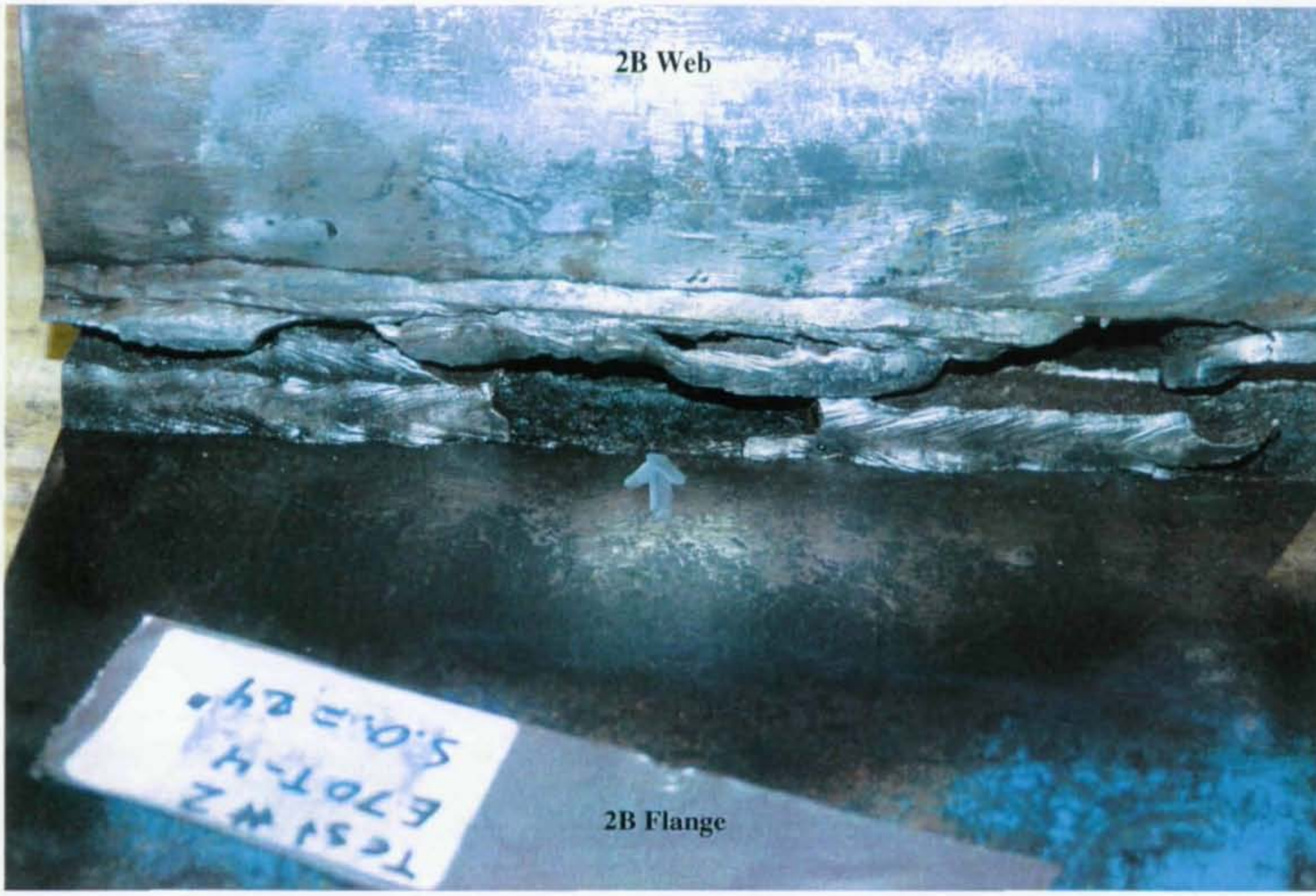

Figure 3. Fracture initiation at the web and flange of Side B in Specimen 2.

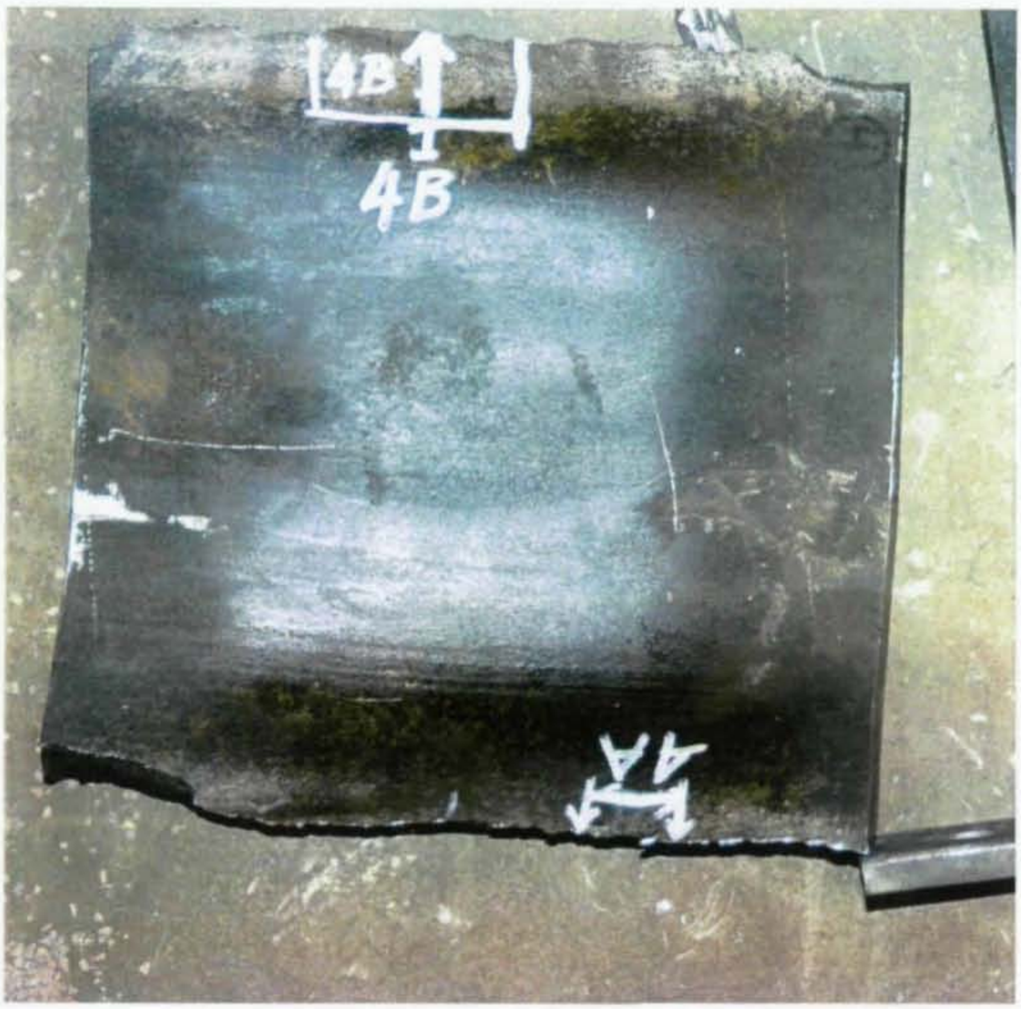

Figure 4. Fracture initiations on both sides of Specimen 4 web.

Figure 5. Fracture initiation on Flange A of Specimen 5.

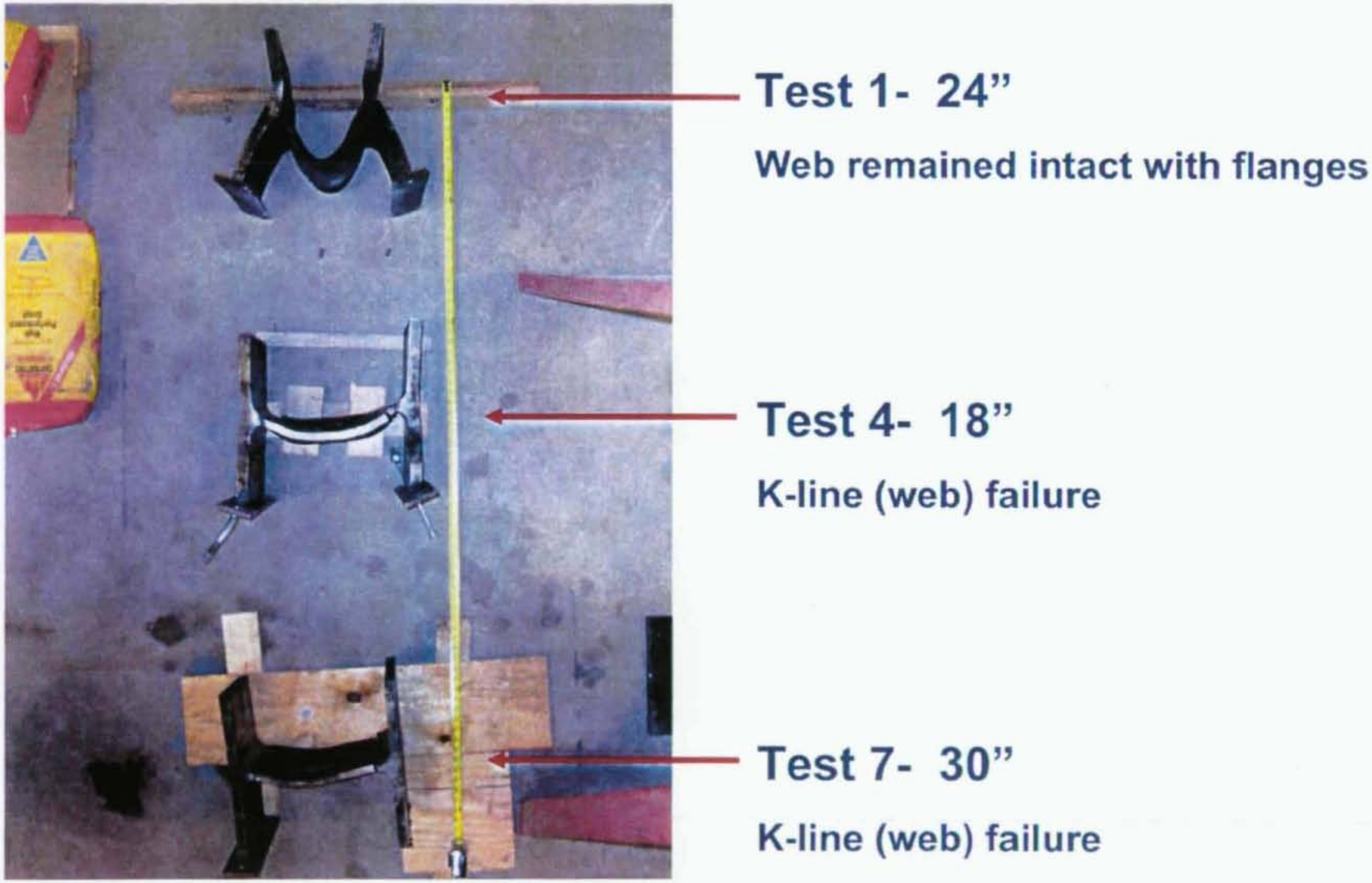

Figure 6. Comparison of results for blast tested rolled structural shape specimens [1].

Figure 7.1 Fracture A 1.7X.

Figure 7.2. Fracture B 1.7X

Figure 7. General views of Fractures A and B in Specimen 4.

initiation

Figure 8.1. Fracture A 2.2X.

Figure 8.2. Fracture B 2.2X.

Figure 8. General views of Fractures A and B in Specimen 7

Figure 9. Transverse cross section through Fracture A in Specimen 4. 3.2X.

Figure 10. Transverse cross section through fracture initiation site in Fracture B of Specimen 7. 4.3X.

Initiation

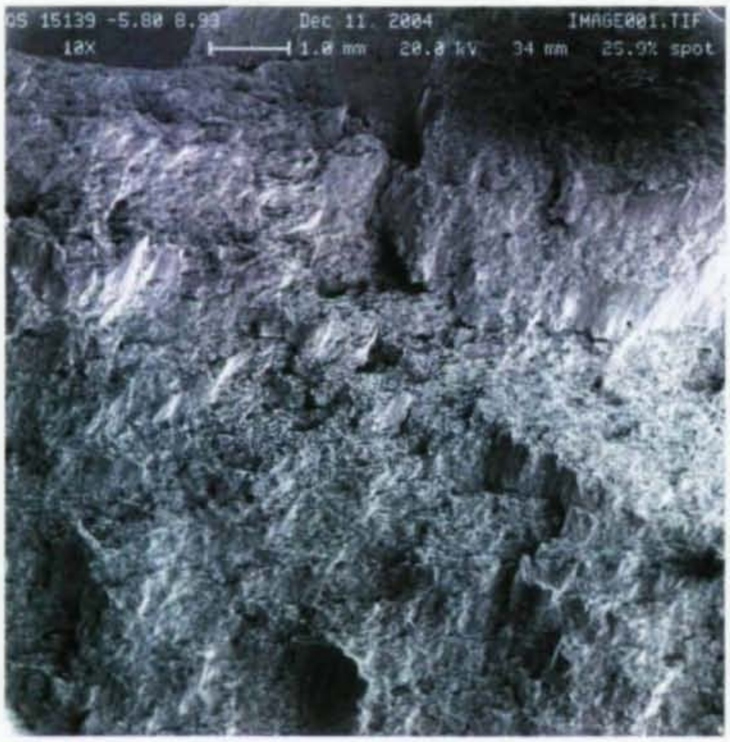

Figure 11.1 10X.

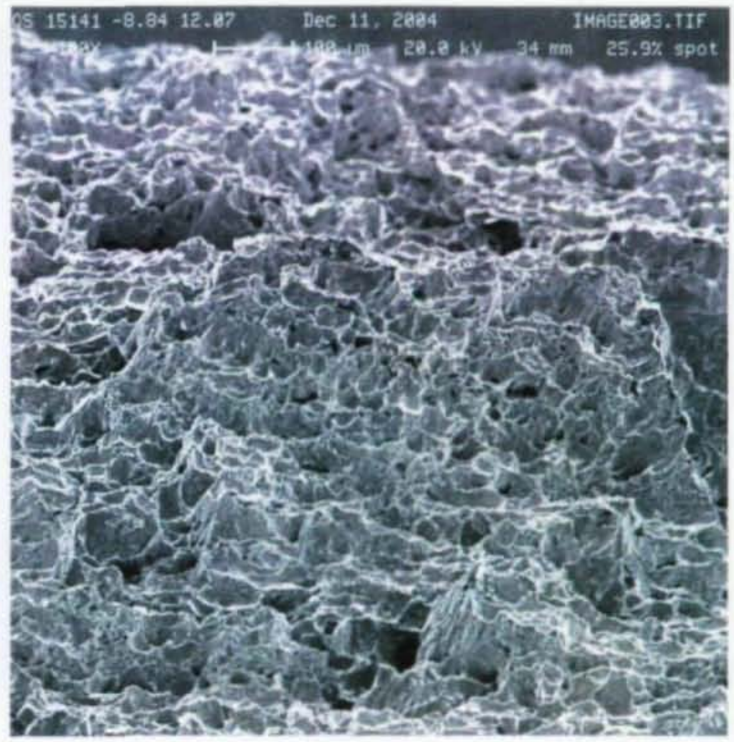

Figure 11.2. 100X.

Initiation

Figure 11.3. 10X.

Figure 11.4. 100X.

Terminal Fracture

Figure 11. Scanning-electron images of ductile shear initiation and terminal fracture in Fracture A of Specimen 4.

Initiation

Figure 12.1. 17X.

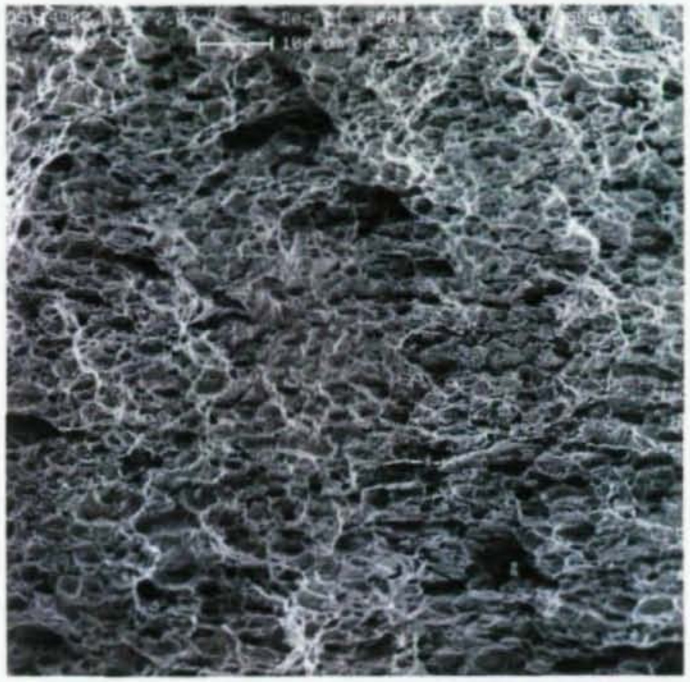

Figure 12.2. Ductile shear initiation 100X.

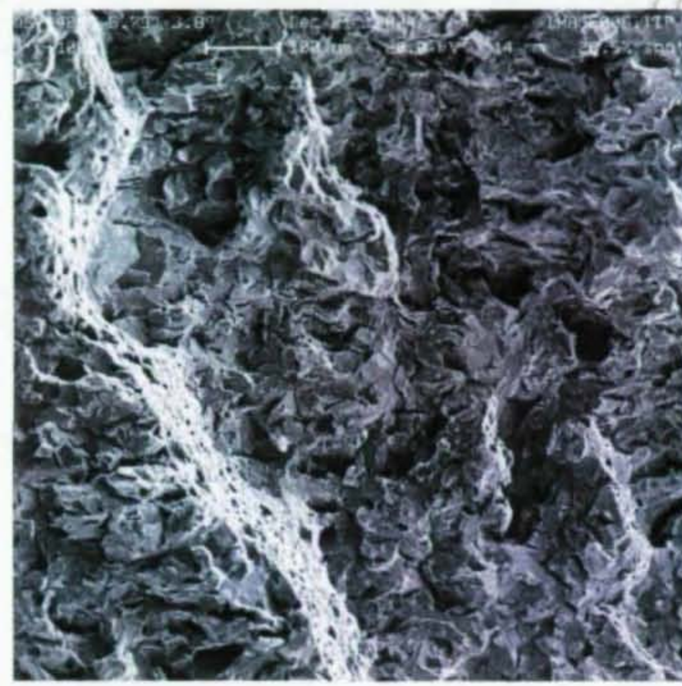

Figure 12.3. Cleavage propagation 100X.

Figure 12.4. Terminal mixed mode fracture 100X.

Figure 12. Scanning-electron images of Fracture B in Specimen 7.

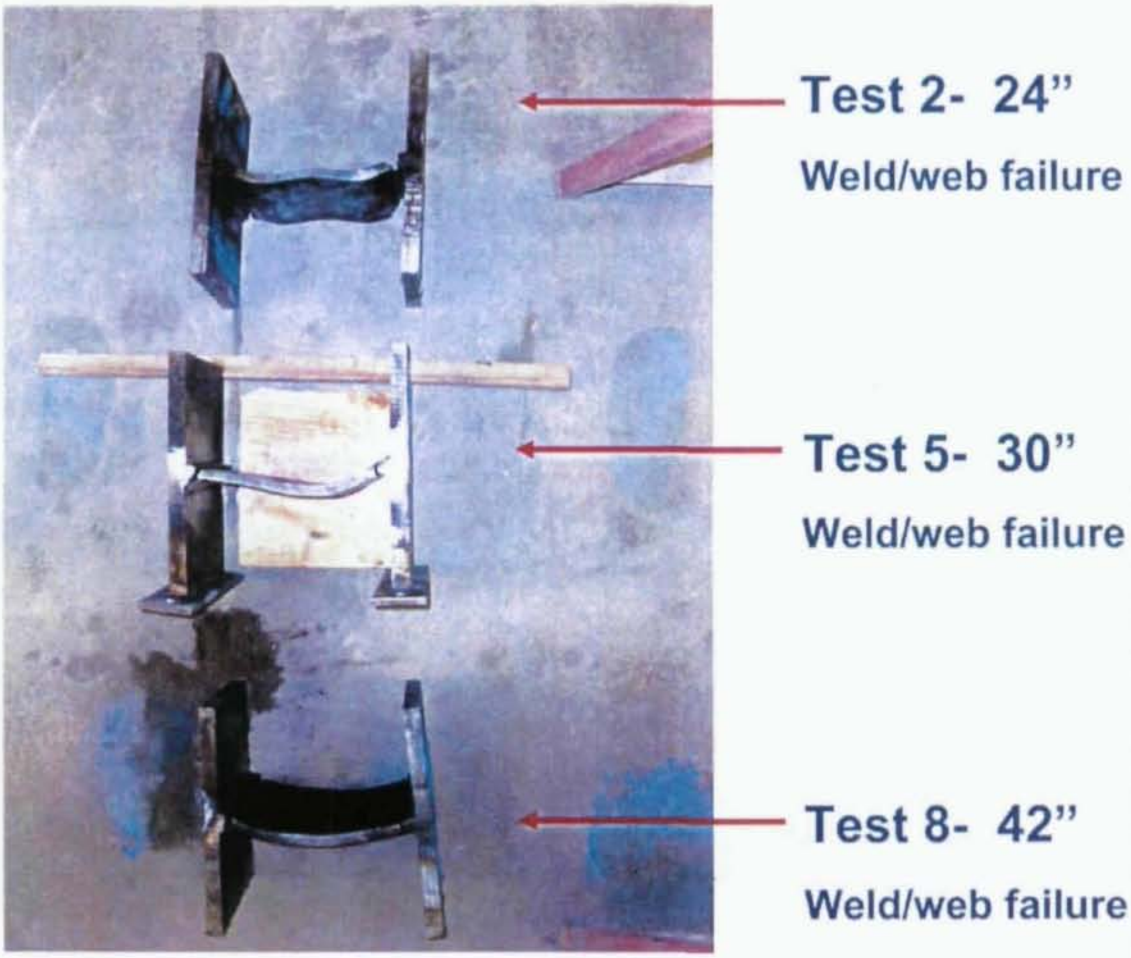

Figure 13. Comparison of results for blast tested specimens welded with E70T-4 electrode [1].

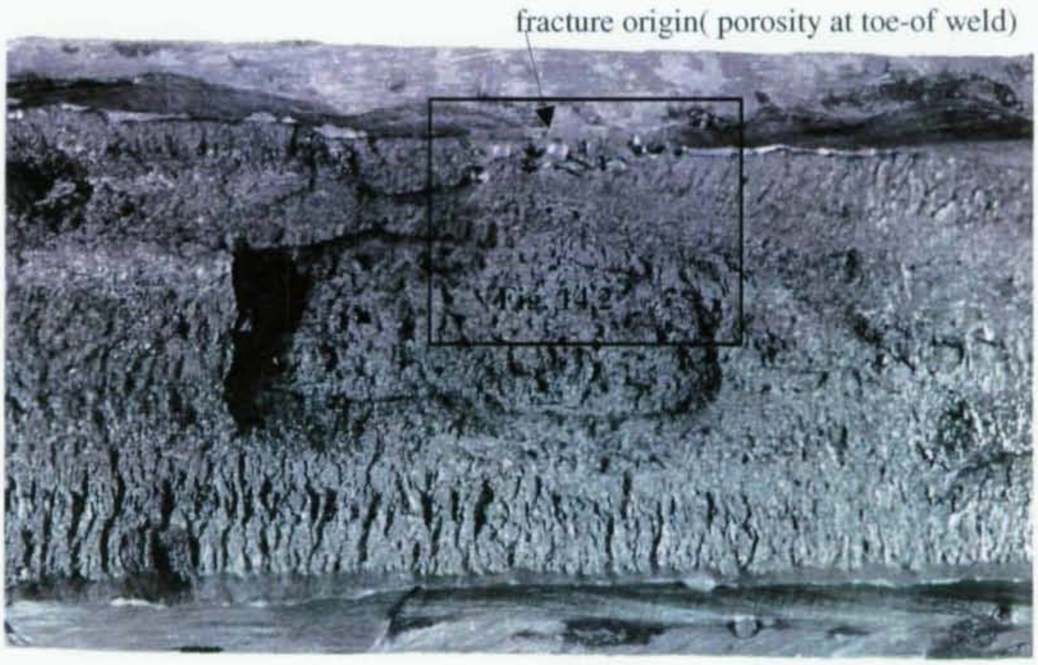

Figure 14.1. Close up images of initiation of Fracture A in Specimen 2. 2X.

Figure 14.2. Higher magnification image of Fracture A initiation site in Specimen 2. 5.4X.

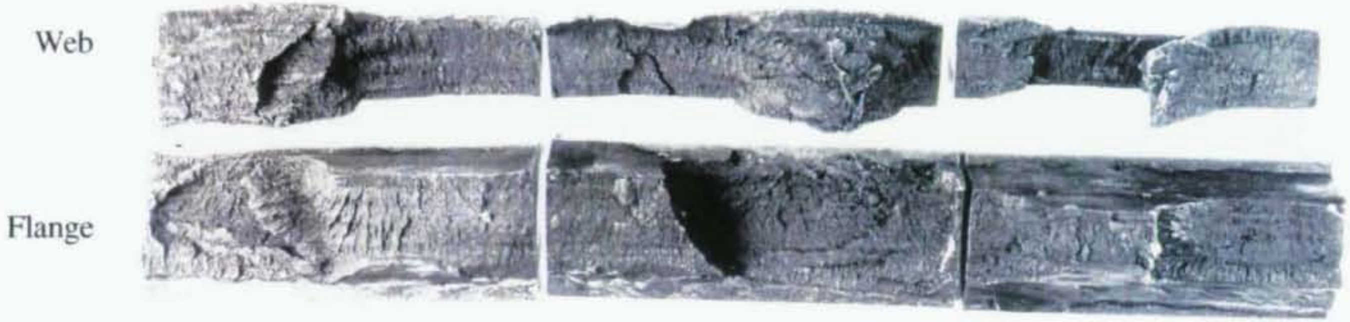

0.48X.

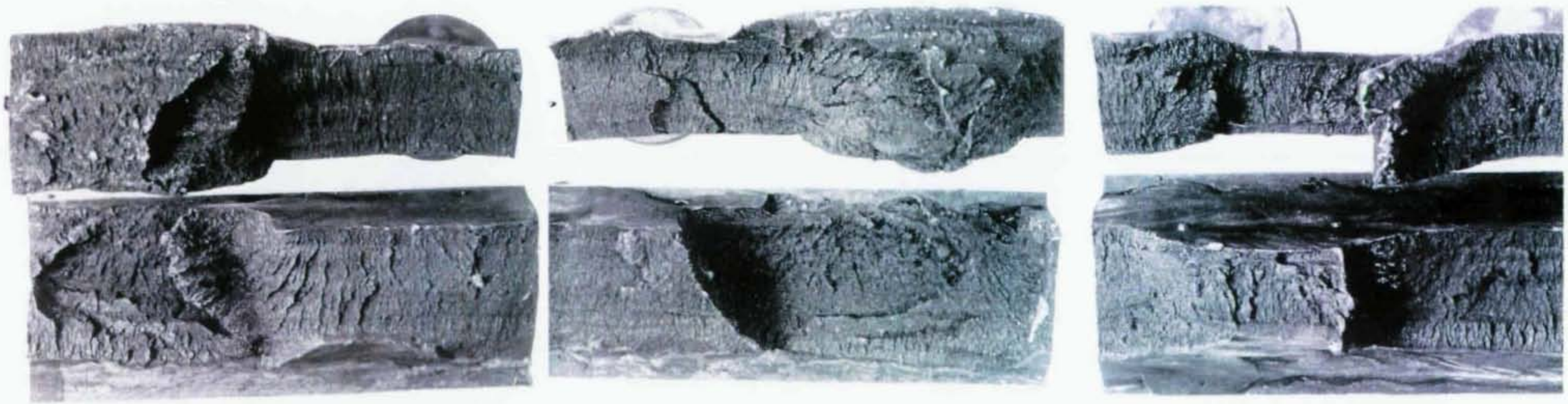

Figure 14.3. Close up images at increasing magnification of Fracture B in Specimen 2 showing multiple initiation sites. 0.75X.

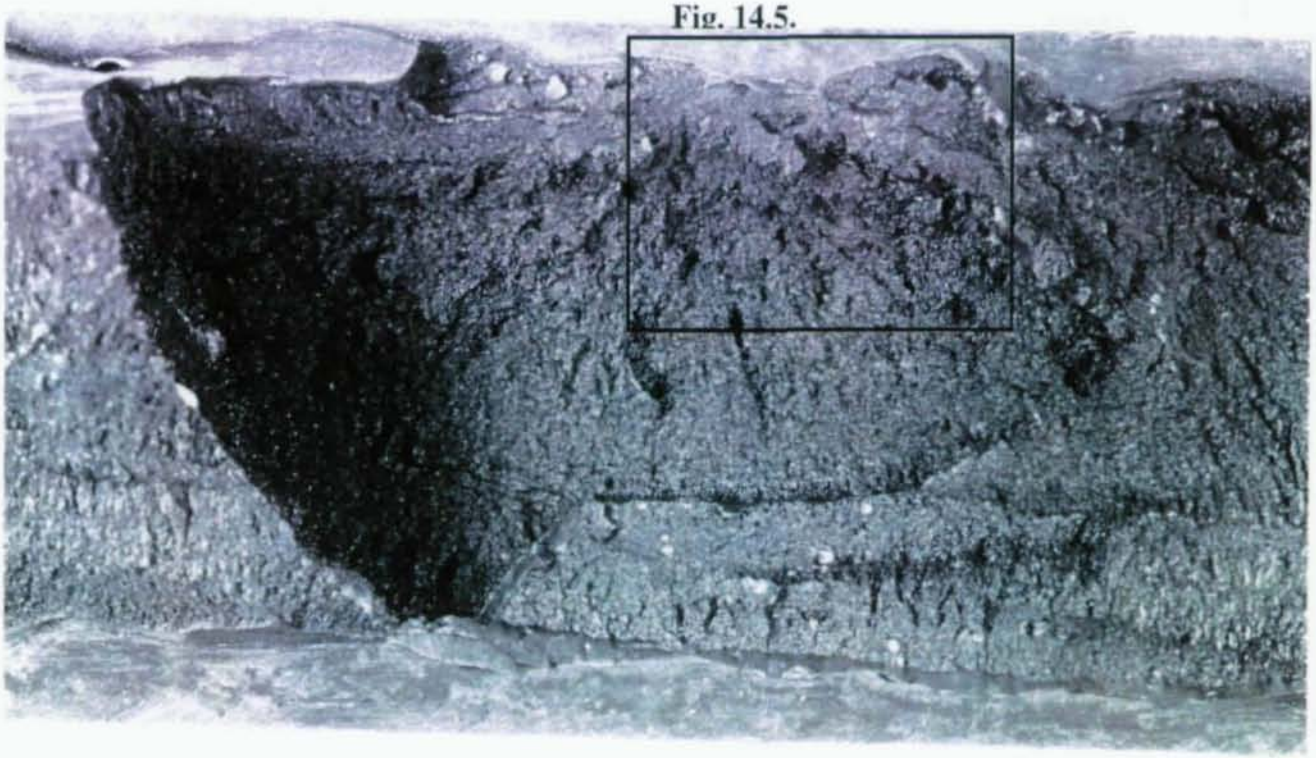

Figure 14.4 2.2X.

Figure 14.5. 5.4X

Figure 14. Higher magnification images of Fracture B initiation site in Specimen 2.

Figure 15.1 1.3X.

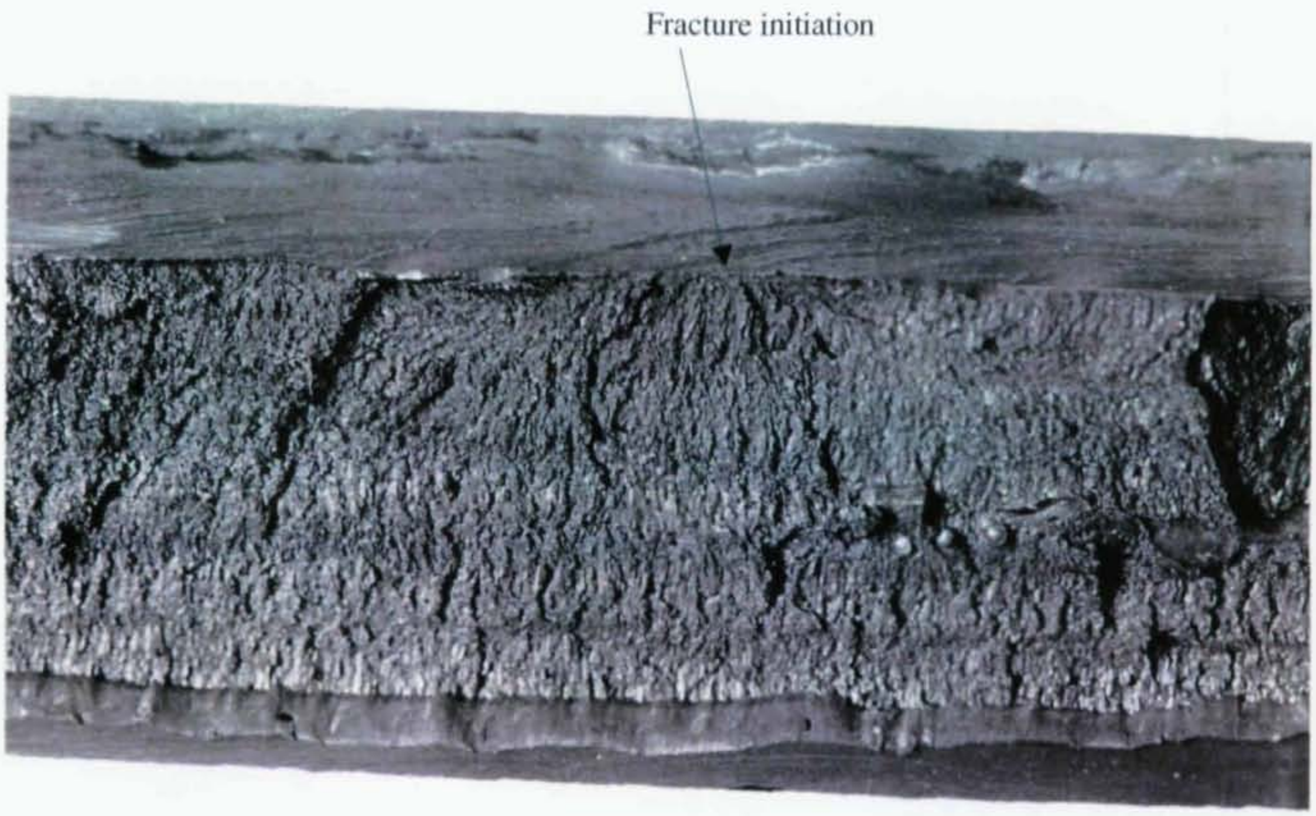

Figure 15.2. 2.4X.

Figure 15. General views of Fracture A in Specimen 5

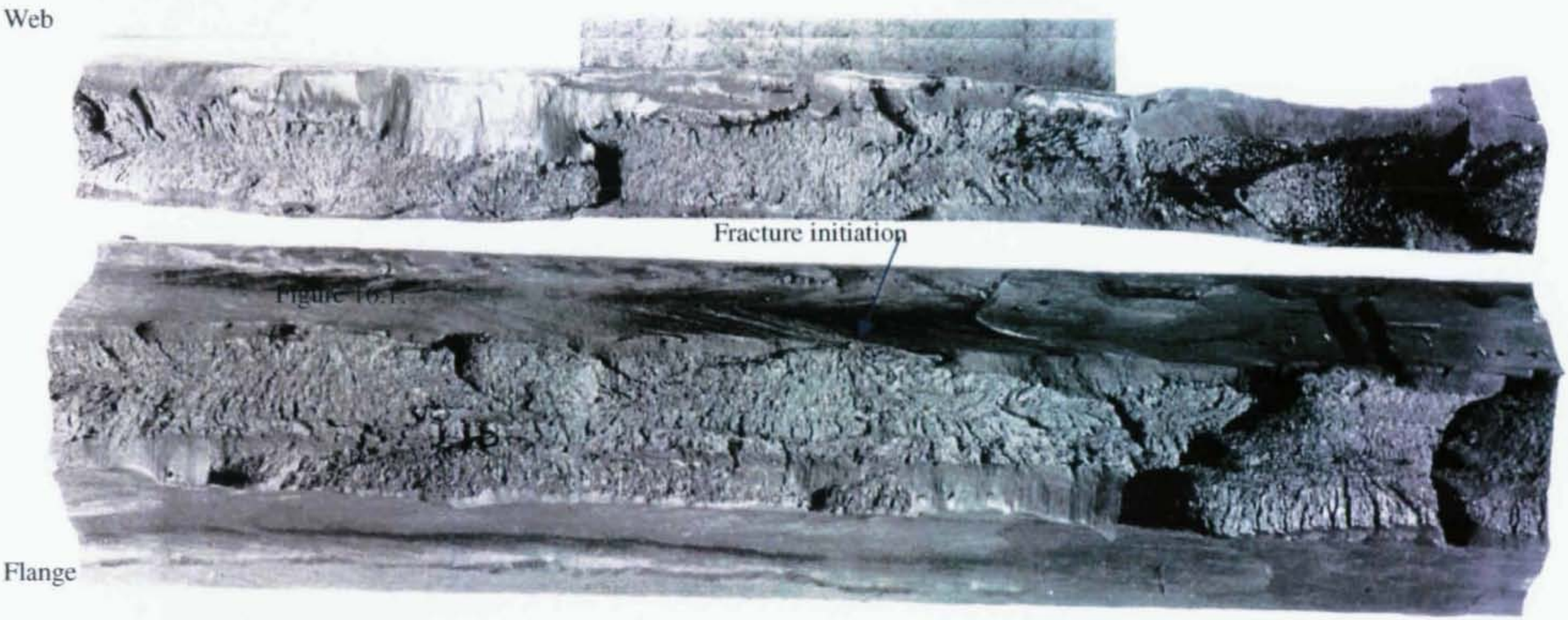

Figure 15.3. General views of Fracture B in Specimen 5. 1.4X.

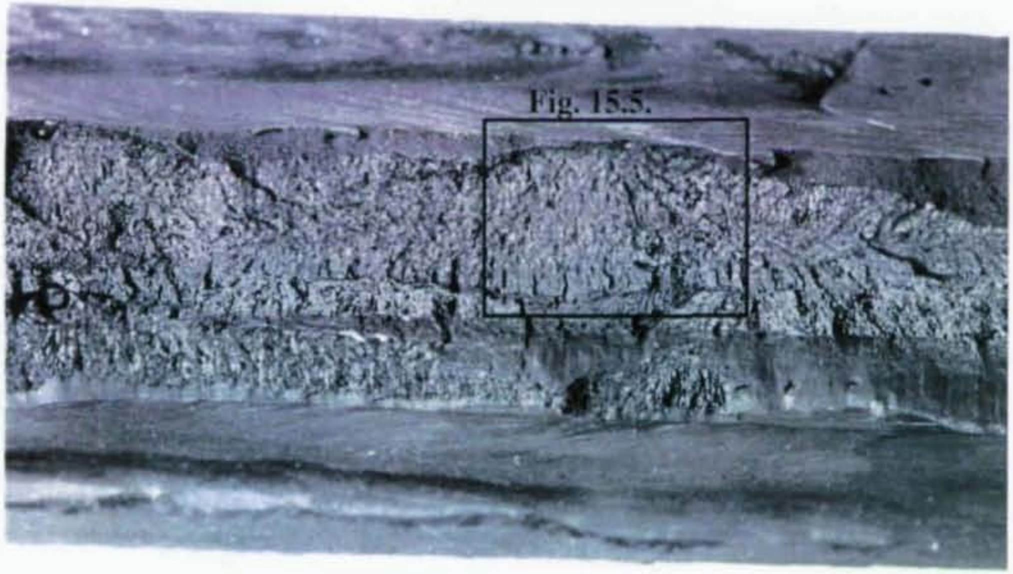

Figure 15.4. 1.8X.

Fracture origin

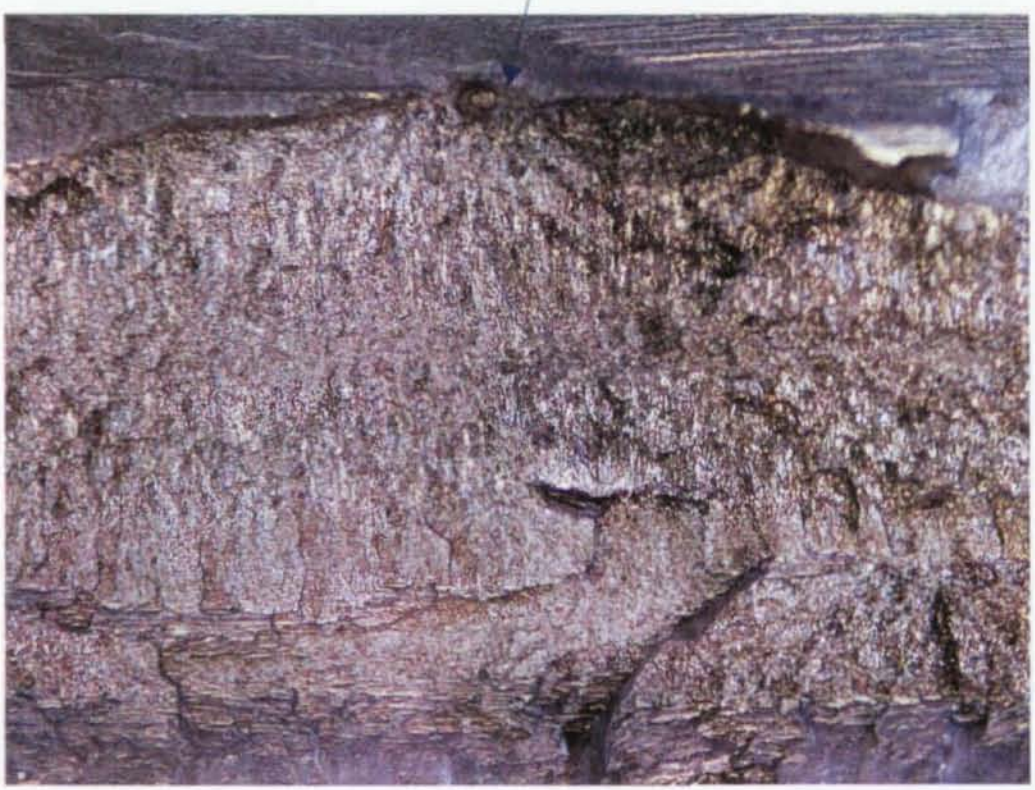

Figure 15.5. Higher magnification images of Fracture B in Specimen 5 showing initiation at porosity in weld. 5.4X.

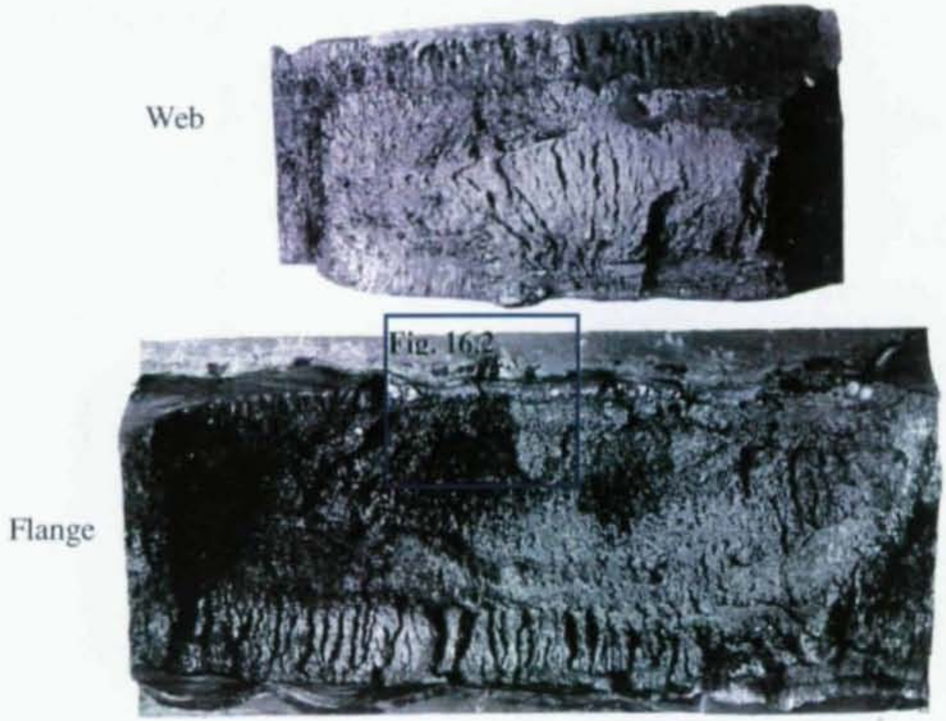

Figure 16.1. 0.9X.

Figure 16.2. 5.4X.

Figure 16. General and close up views of fracture initiation in Fracture A in Specimen 8.

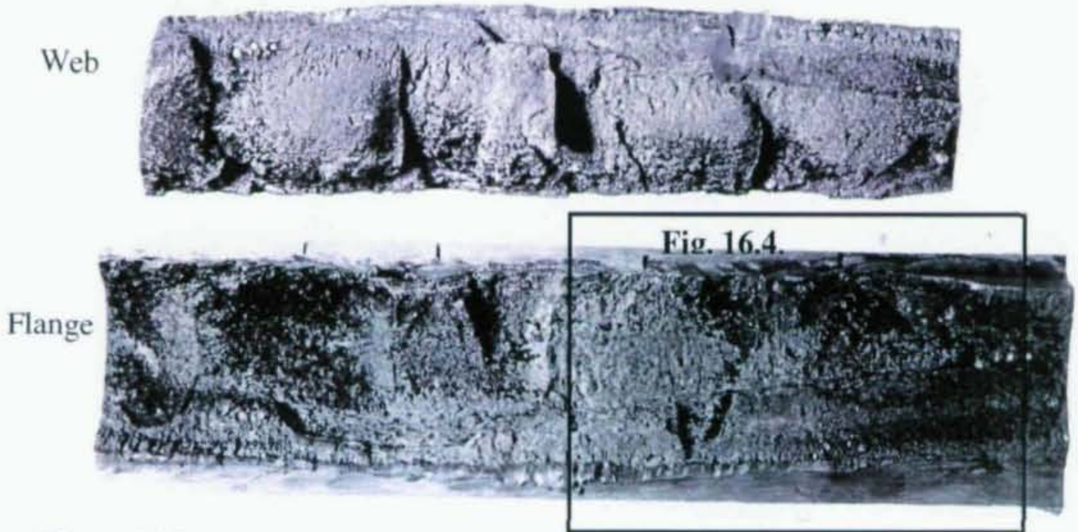

Figure 16.3. 0.8X.

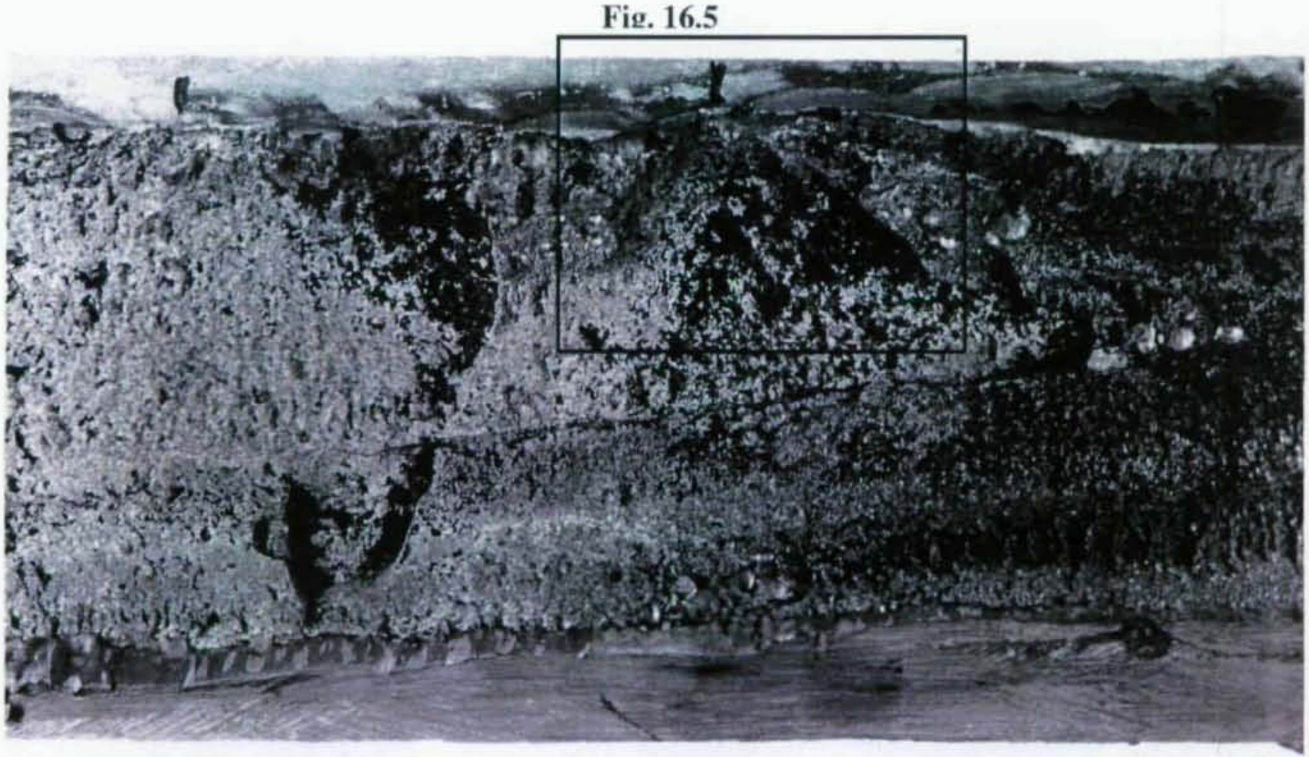

Figure 16.4. 2.2X.

Figure 16. General and close up views of fracture initiation in Fracture B in Specimen 8

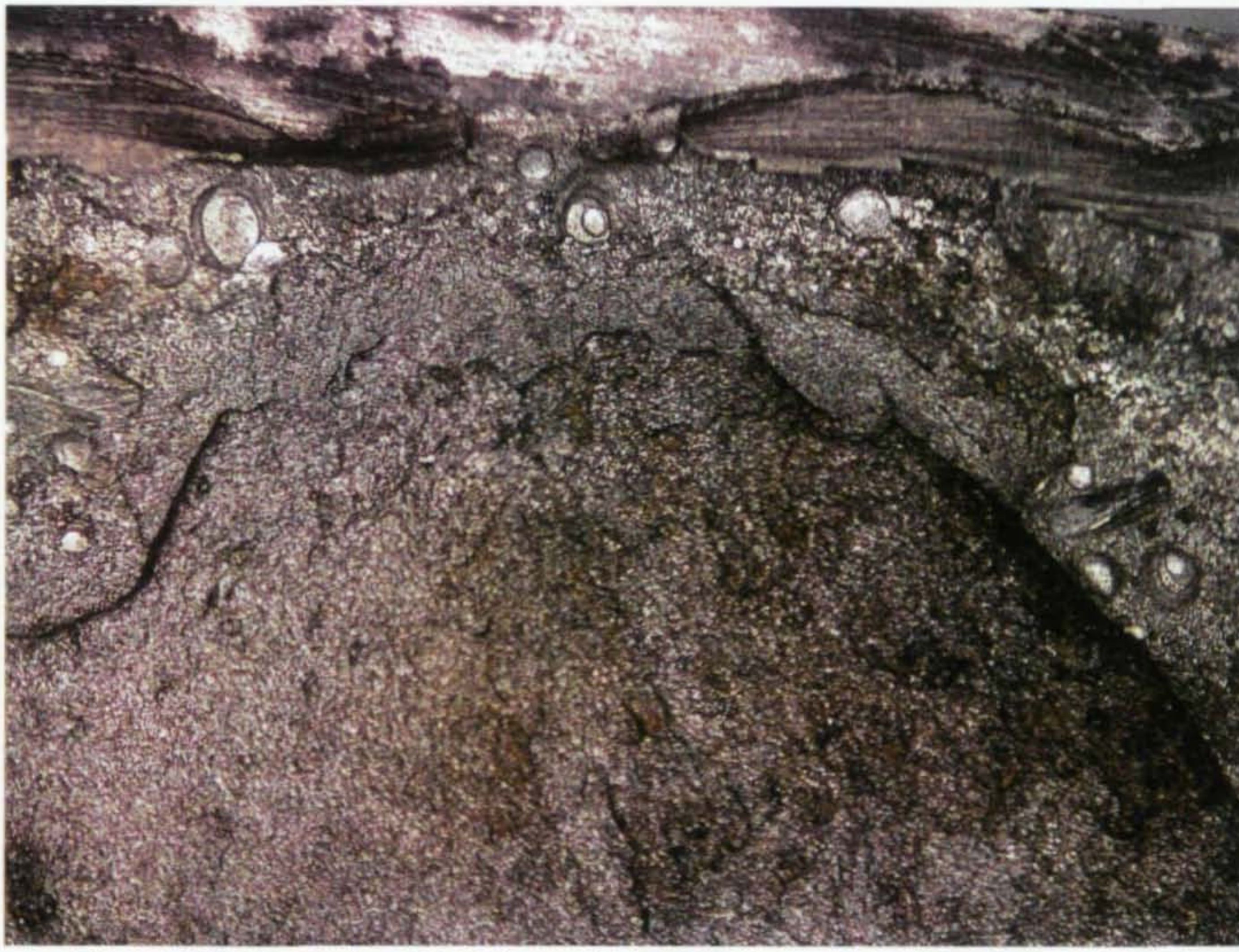

Figure 16.5. Close up view of local fracture initiation site in Fracture B of Specimen 8. 8.5X.

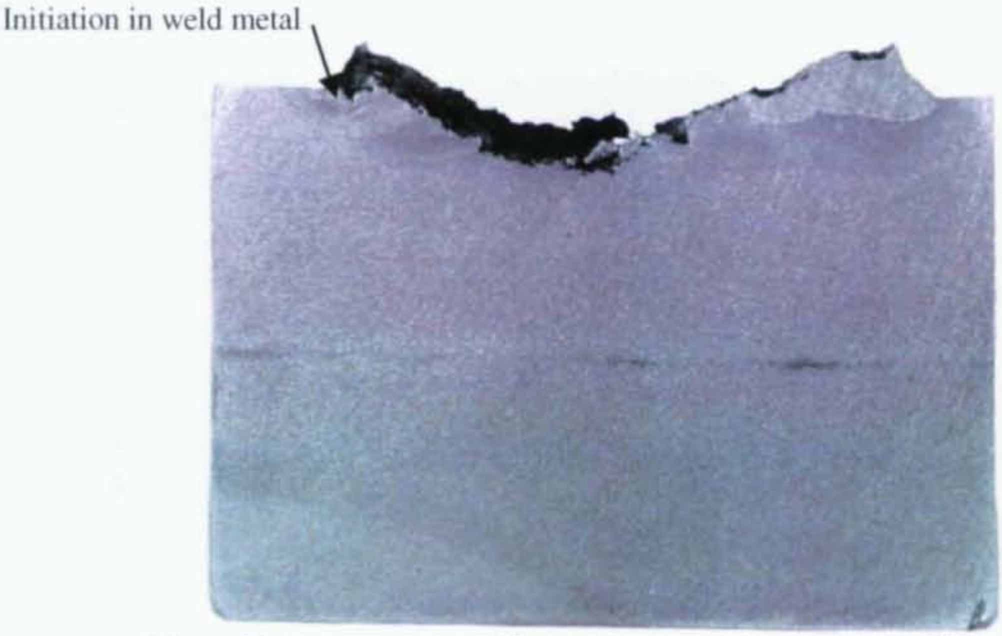

Figure 17.1. Fracture A 2.7X.

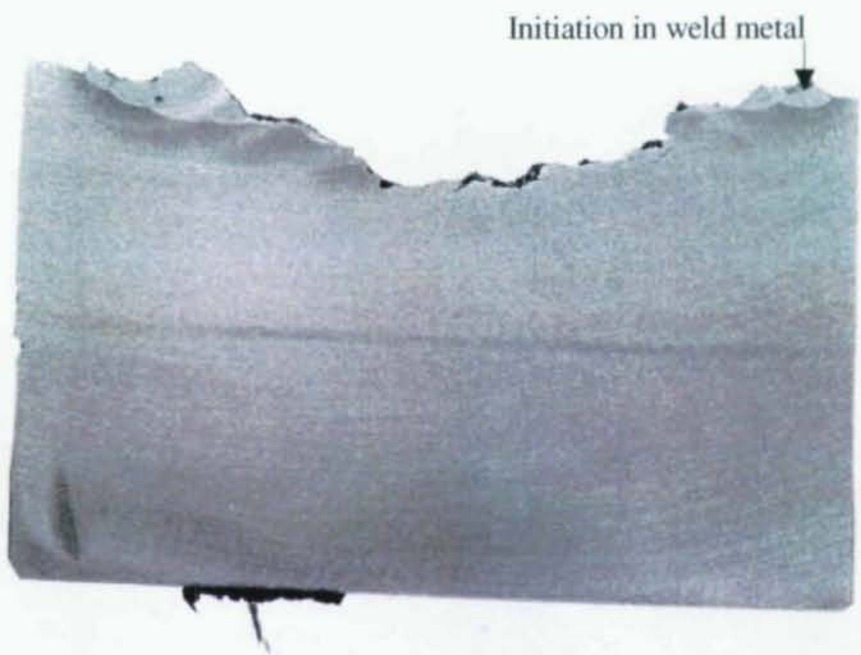

Figure 17.2. Fracture B 2.7X.

Figure 17. Transverse cross sections through fracture initiation sites in Specimen 2.

Initiation between passes in weld metal

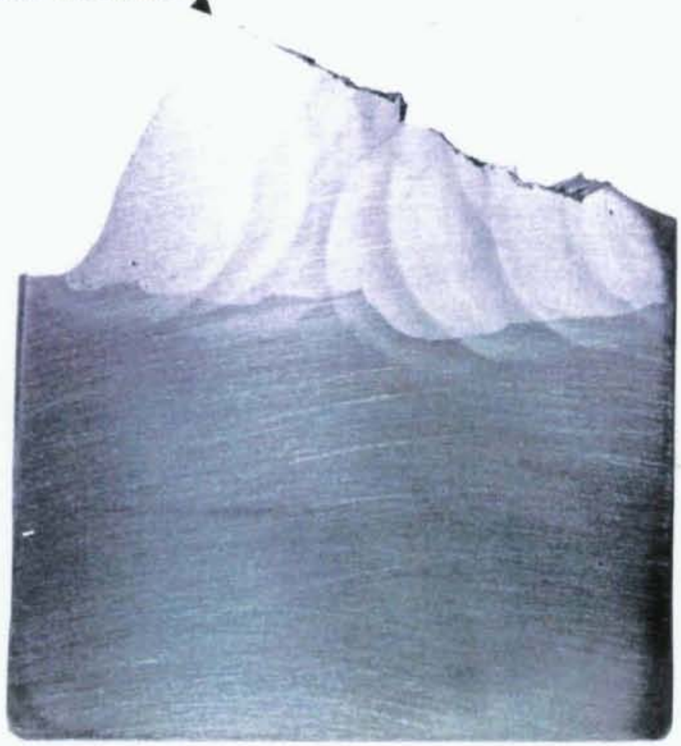

Figure 18.1. Fracture A 2.2X.

Initiation at porosity between weld passes

Figure 18.2. Fracture B 2.2X

Figure 18. Transverse cross sections through fracture initiation sites in Specimen 5.

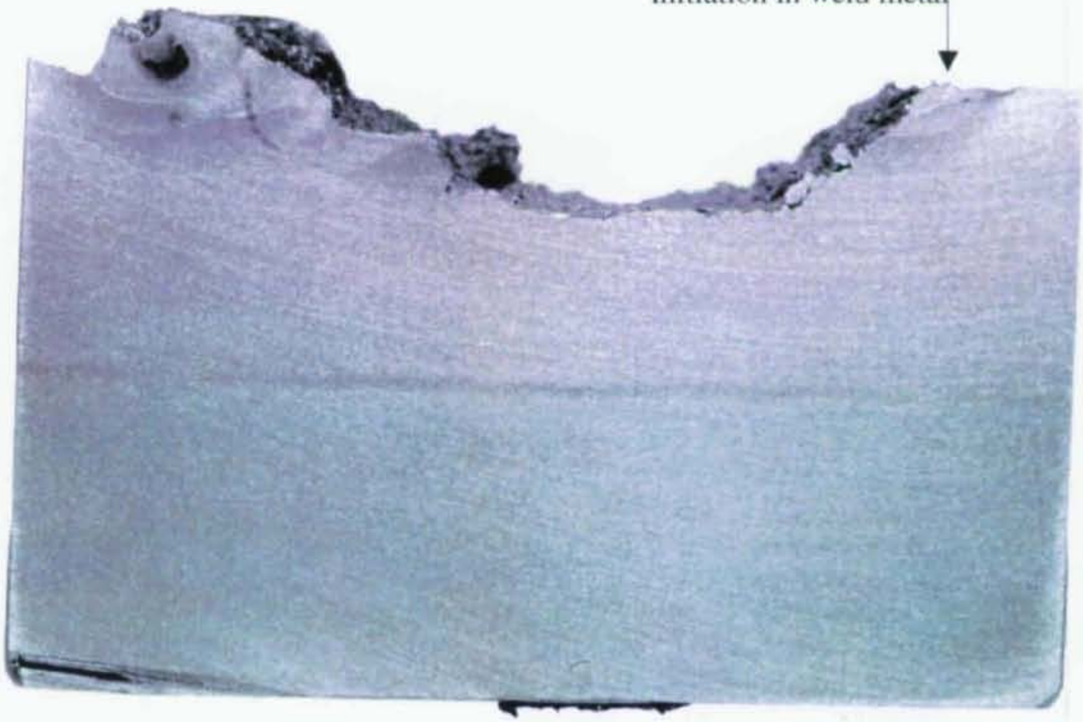

Figure 19.1. Fracture A. 3.2X.

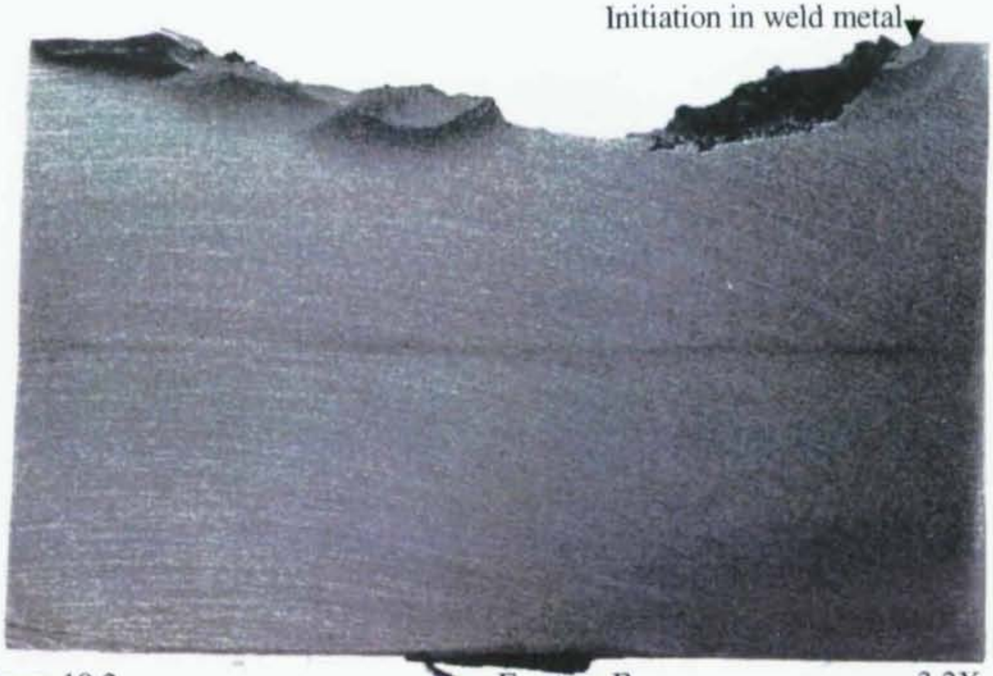

Figure 19.2. Fracture B. 3.2X.

Figure 19. Transverse cross sections through initiation sites in Specimen 8.

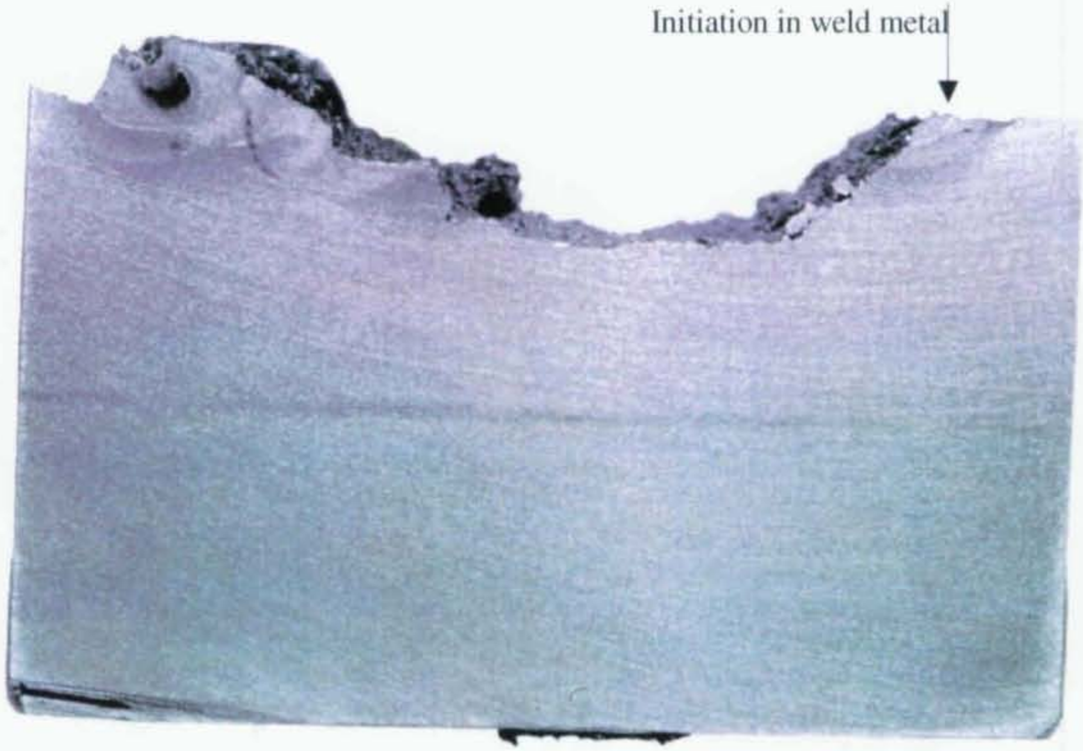

Figure 19.1. Fracture A. 3.2X.

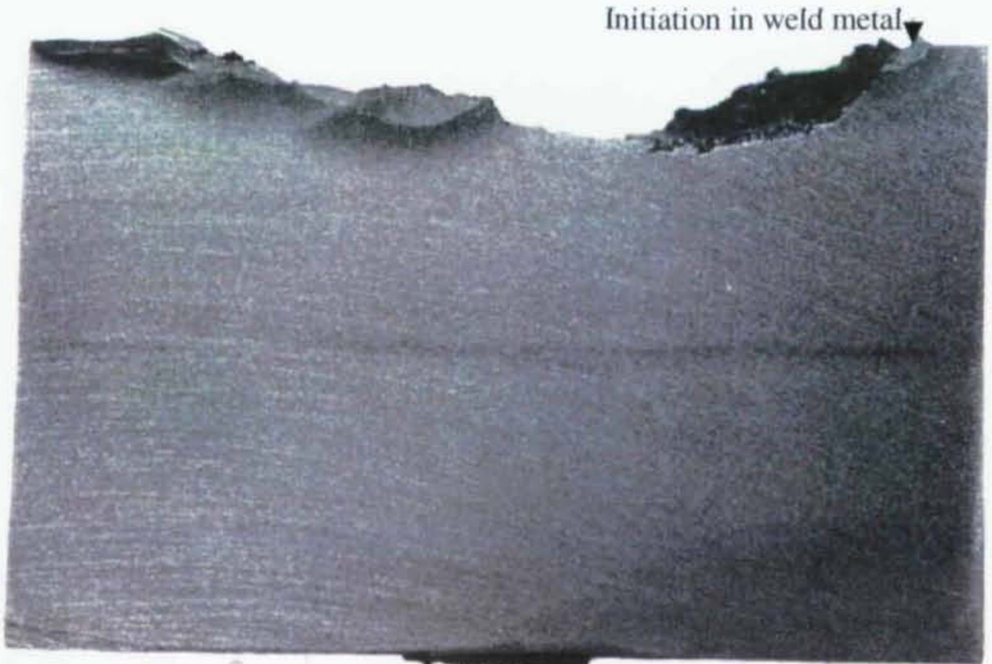

Figure 19.2. Fracture B. 3.2X.

Figure 19. Transverse cross sections through initiation sites in Specimen 8.

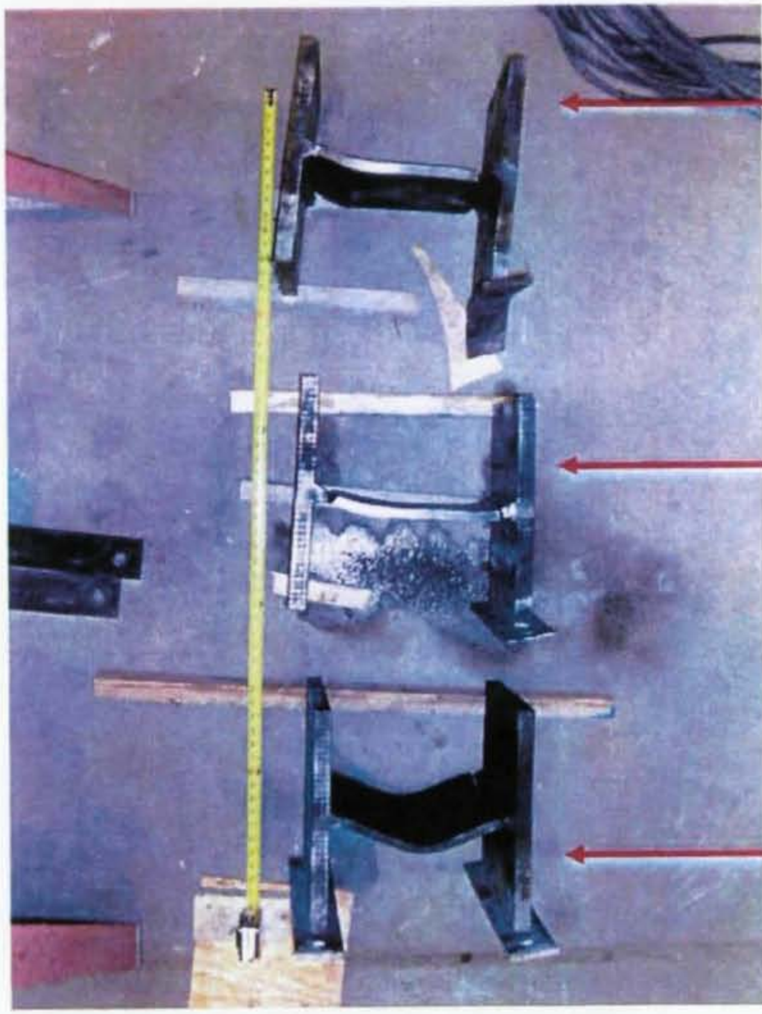

Test 3- 24"

Weld failure both ends of web

Test 6- 30"

Weld failure both ends of web

Test 9- 42"

Partial failure (Weld fracture only at one end of web)

Figure 20. Comparison of results for blast tested specimens welded with E70T-6 electrode [1].

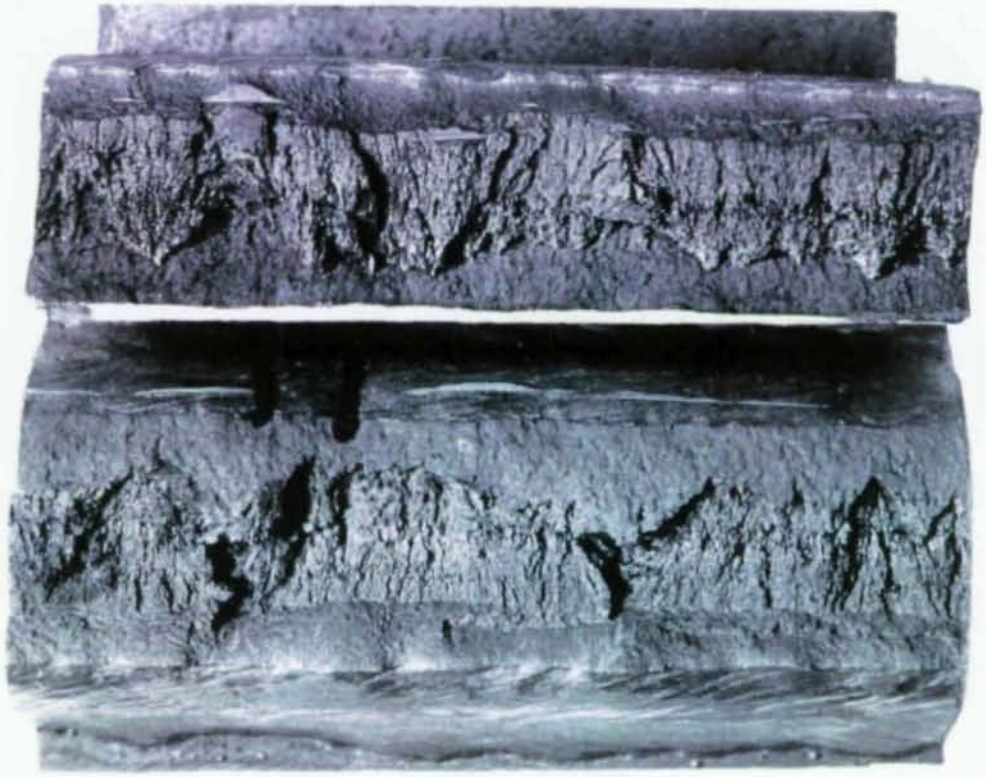

Figure 21.1. 1.65X.

Figure 21.2. 2.25X.

Figure 21. General views of Fracture A in Specimen 3

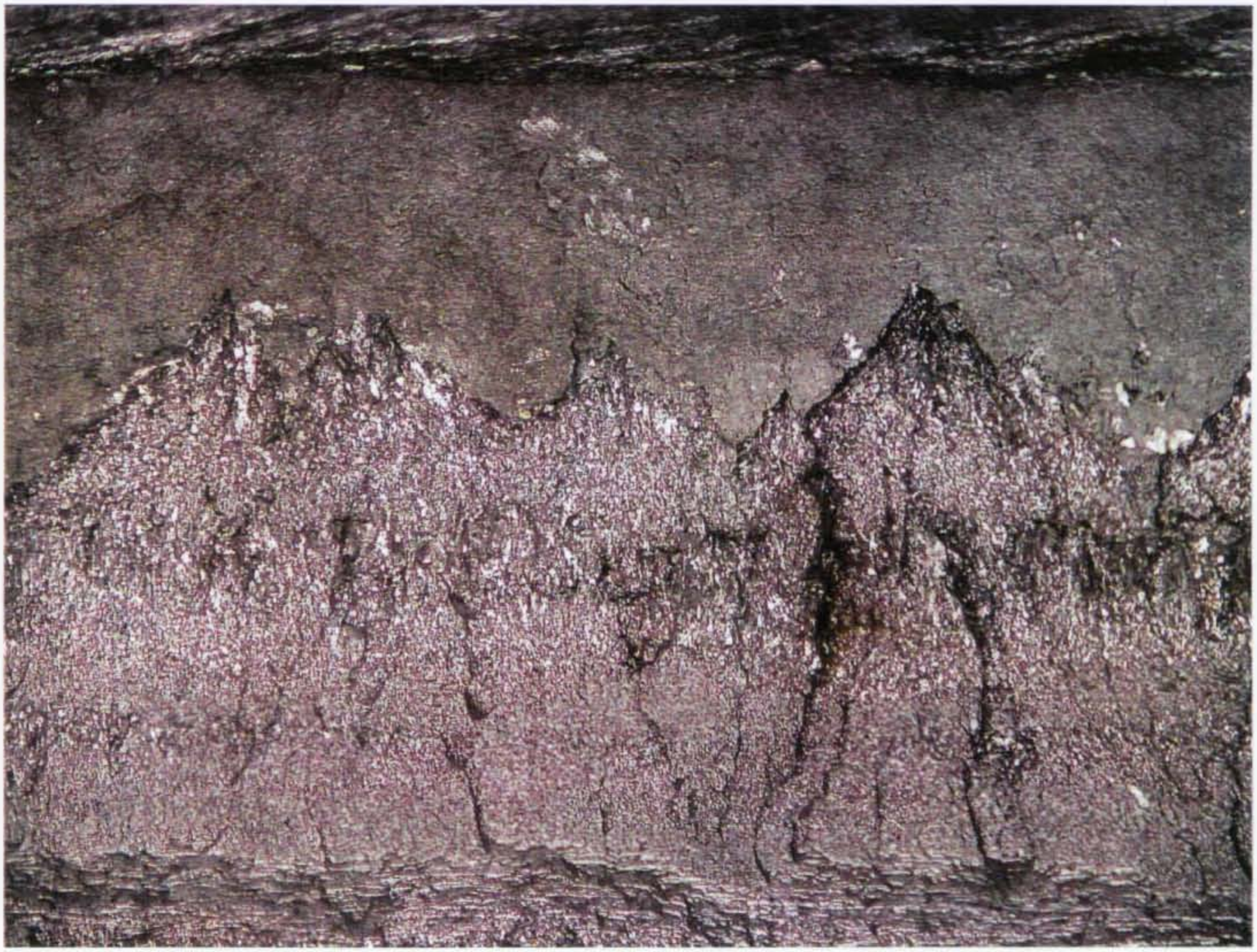

Figure 21.3. Close up view of Fracture A in Specimen 3. 7X.

Web

Flange

Figure 21.4. 1.65X.

Figure 21.5. 2.25X.

General views of Fracture B in Specimen 3.

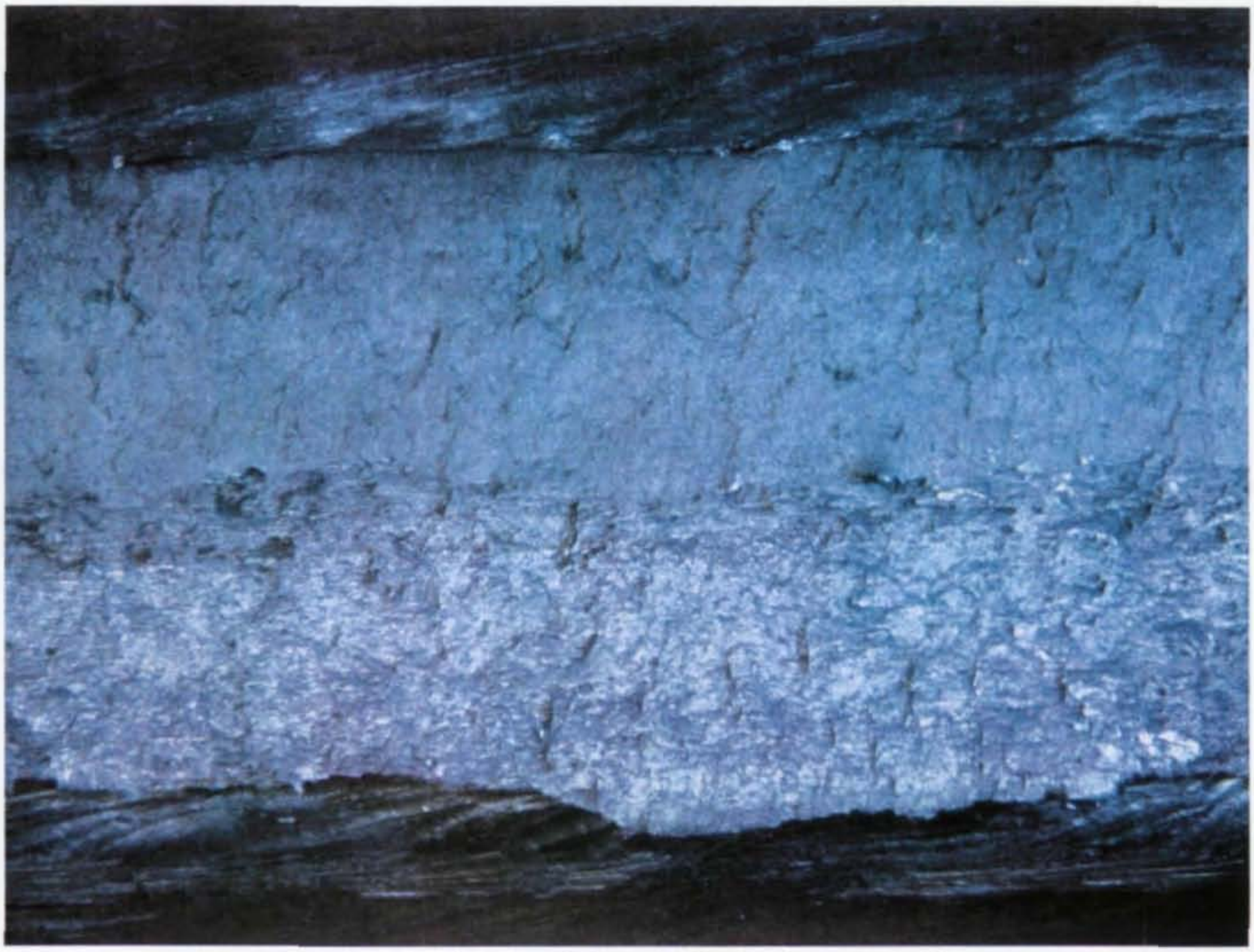

Figure 21.6. Close up of Fracture B in Specimen 3. 5.6X.

Figure 22.1. 1.25X.

Figure 22.2. 2.2X.

Figure 22. General views at increasing magnifications of Fracture A in Specimen 6.

Figure 22.3. Higher magnification image of fracture initiation site in Fracture A in Specimen 6. 9X.

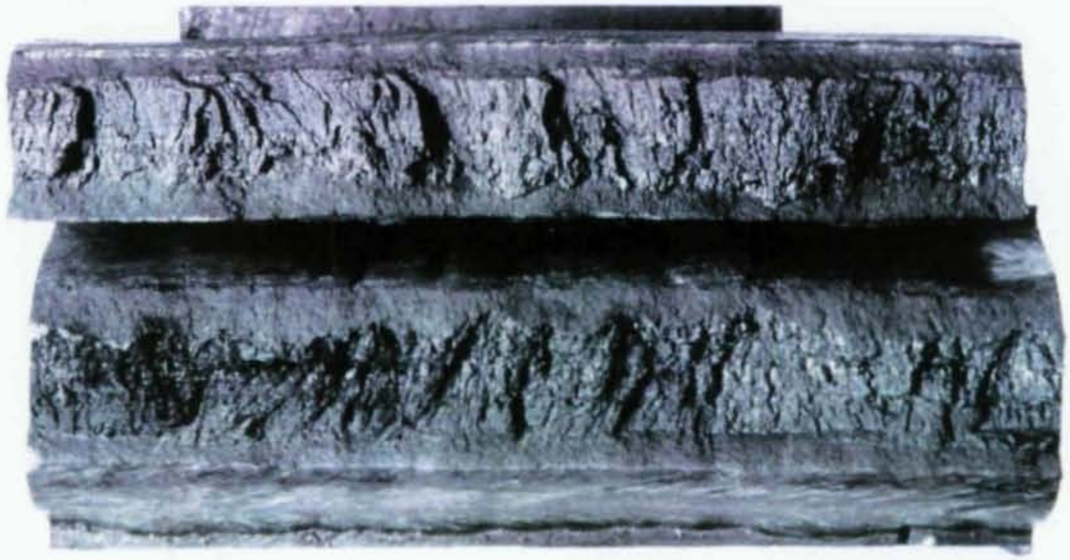

Figure 22.4. 1.25X.

Figure 22.5. 2.2X.

Figure 22. General views of Fracture B in Specimen 6.

Figure 22.6. Higher magnification image of fracture initiation site in Fracture B in Sample 6. 7X.

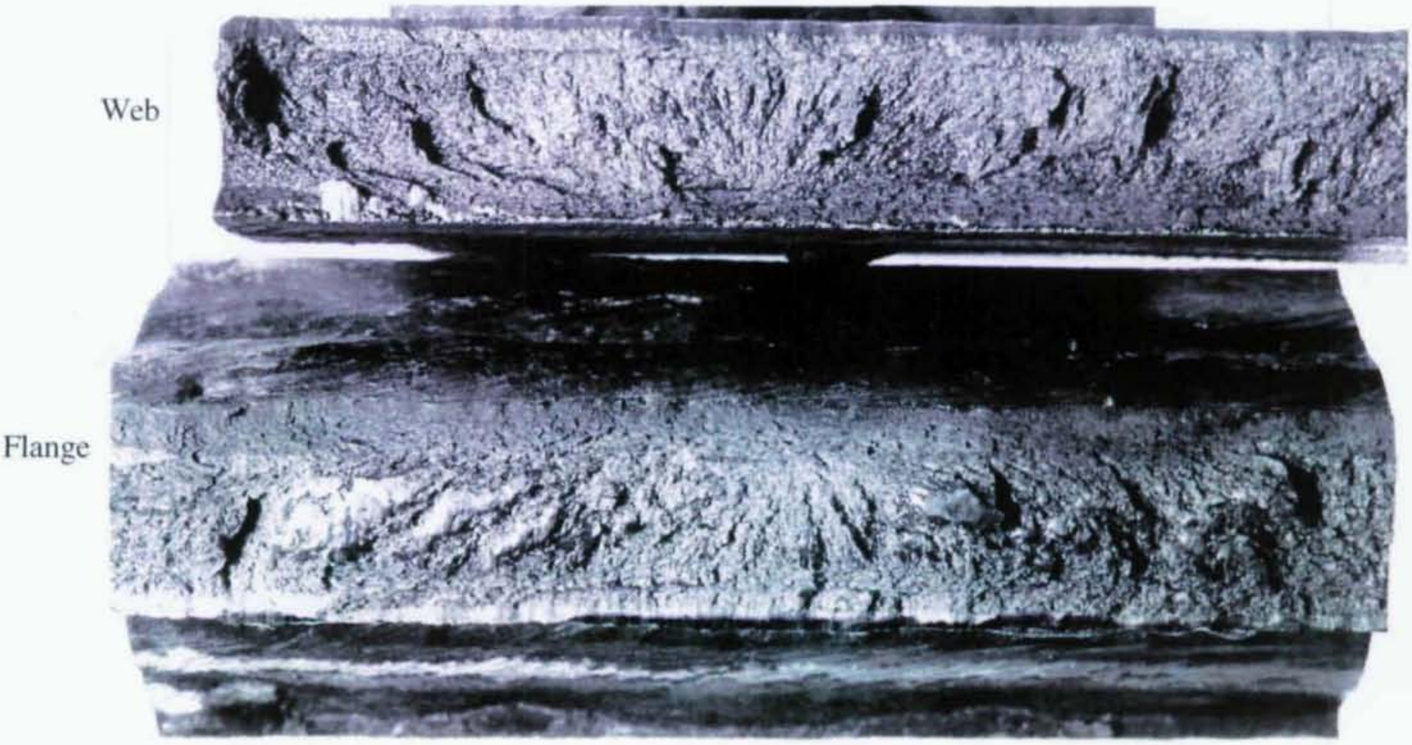

Figure 23.1. 1.65X.

Figure 23.2. 2.4X.

Figure 23. General and close up views of fracture in Specimen 9.

Figure 23.3. Close up of fracture initiation site in Specimen 9. 8X.

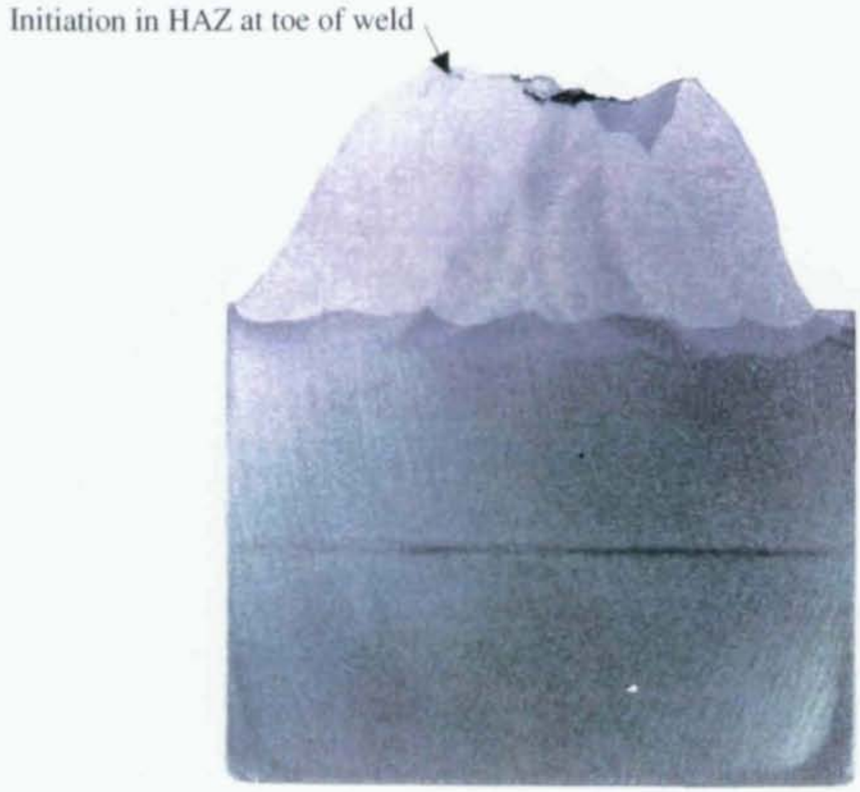

Figure 24.1. Fracture A 2.5X.

Figure 24.2. Fracture B 2.5X.

Figure 24. Transverse cross sections through fracture initiation sites in Specimen 3.

Figure 25.1. Fracture A 2.1X.

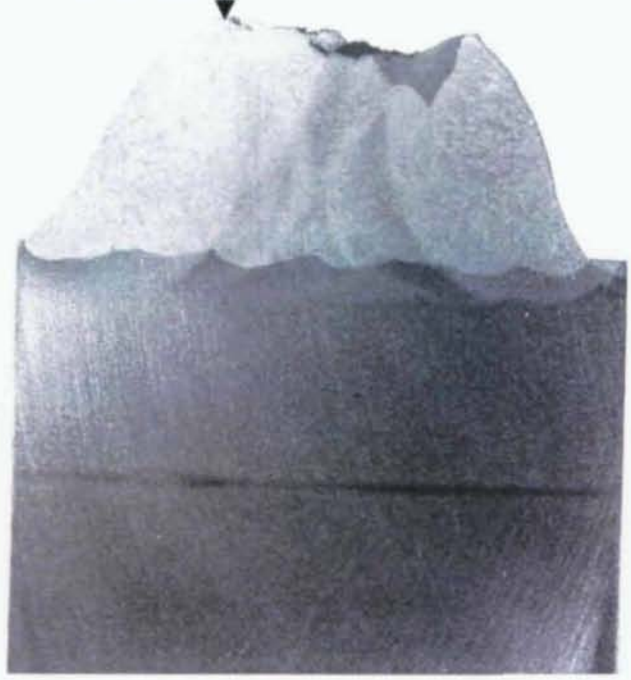

Figure 25.2. Fracture B 2.3X.

Figure 25. Transverse cross section through fracture initiation sites in Specimen 6.

Figure 26. Transverse cross section through fracture initiation site in Specimen 9. 2X.

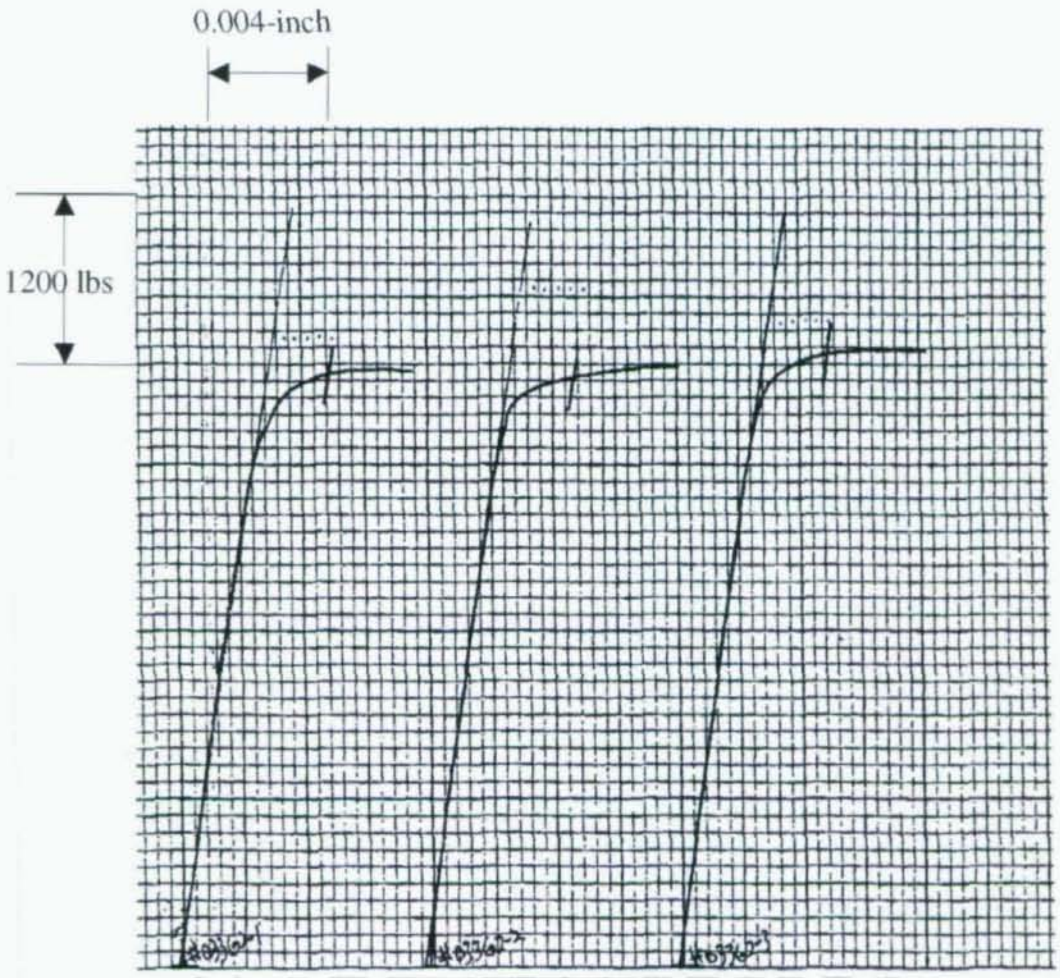

Figure 27. Stress-Strain curves for rolled W14x132 specimen,

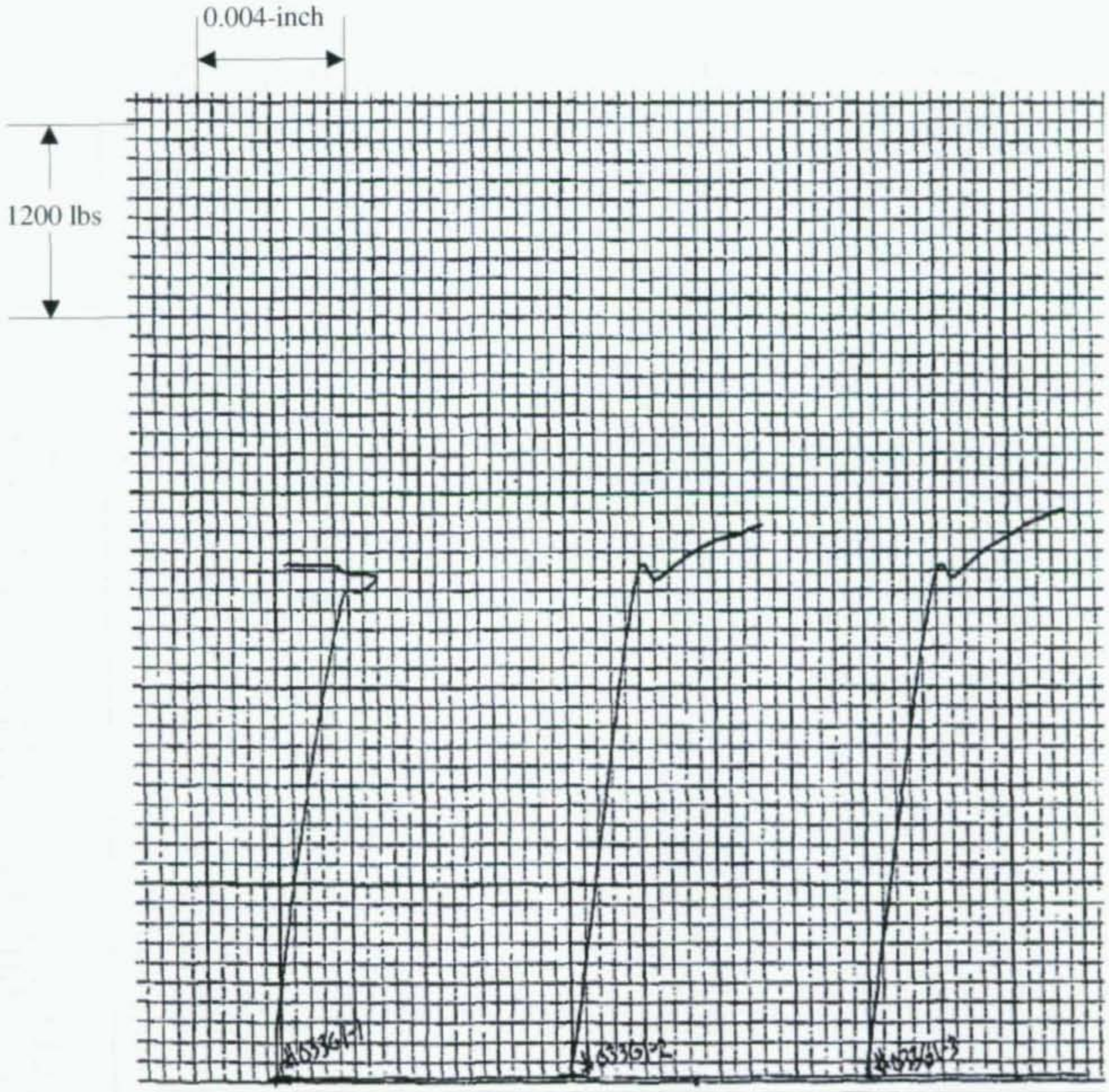

Figure 28. Stress-Strain curve for specimen welded with E70T-4 electrode.

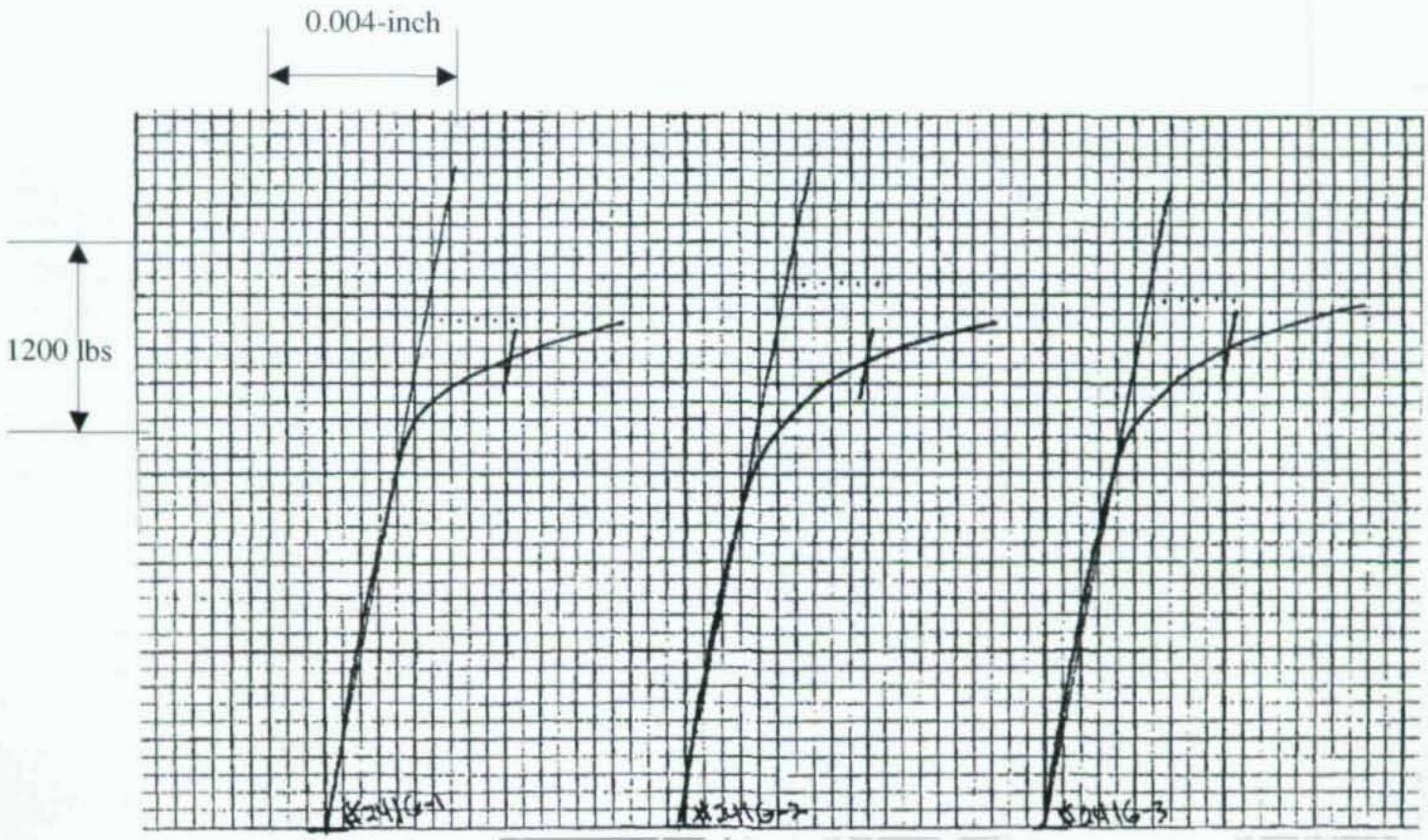

Figure 29. Stress-Strain curve for specimen welded with E70T-6 electrode.

APPENDIX A

General Views of Blast Tested Specimens

Figure 1. General view of as-received test specimens.

Figure 2.1.

Figure 2.2.

General views of Test Specimen No. 1.

Figure 3.1.

Figure 3.2.

Figure 3.3. Fracture 2A

Figure 3.4. Fracture 2B

General views of Fractures A and B in Specimen 2.

Figure 4.1. As-received Specimen 3

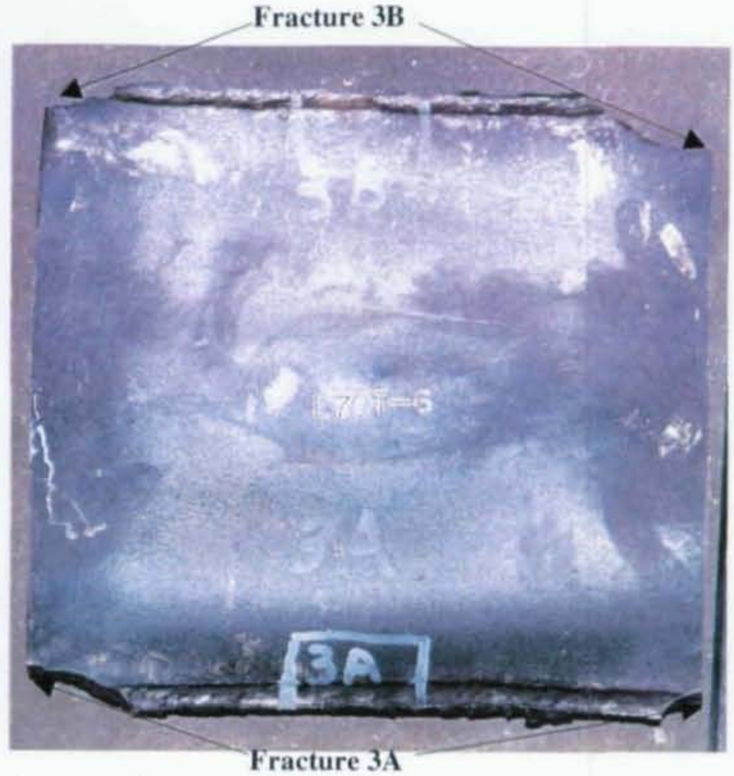

Figure 4.2.

Figure 4.3. Fracture 3A

Figure 4.4. Fracture 3B

General views of Fractures A and B in Specimen 3.

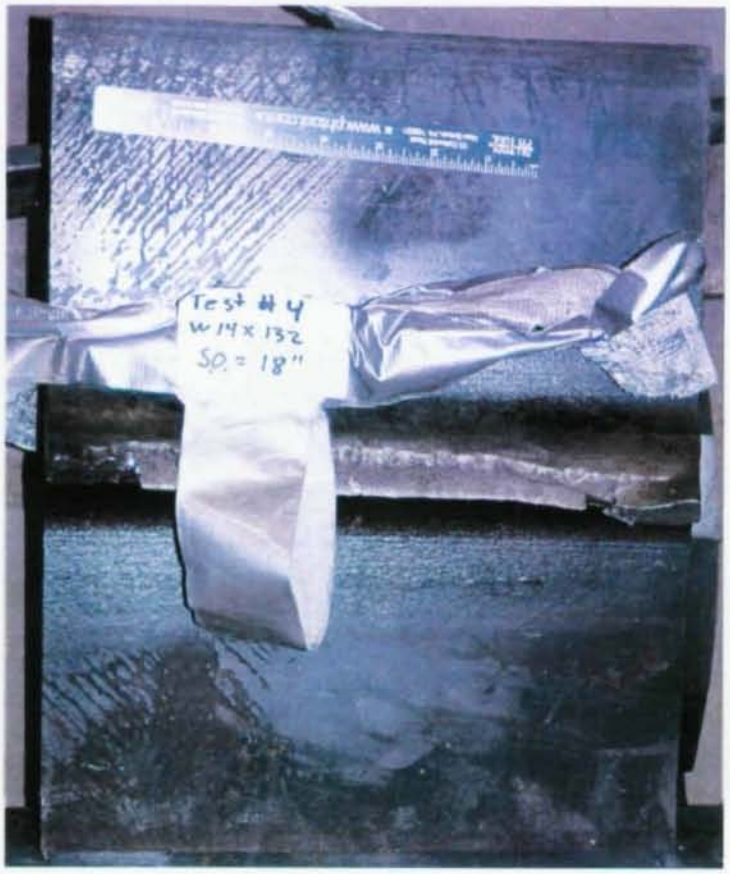

Figure 5.1. As-received Specimen 4

Figure 5.2.

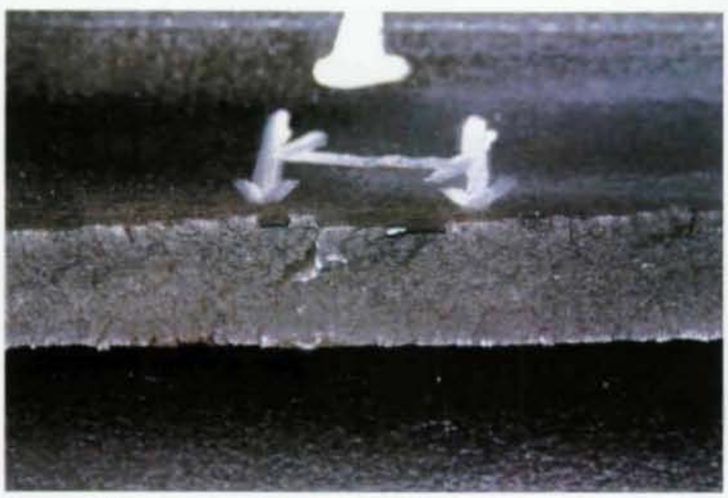

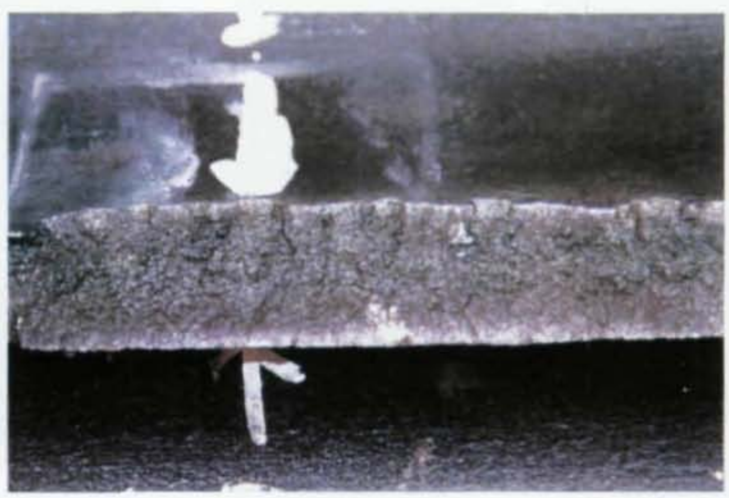

Figure 5.3. Fracture 4A

General views of Fractures A and B in Specimen 4.

Figure 6.1.

Figure 6.2.

Figure 6.3. Fracture 5A

Figure 6.4. Fracture 5B

General views of Fractures A and B in Specimen 5

Figure 7.1.

Figure 7.2.

Figure 7.2. Fracture 6A

Figure 7.3. Fracture 6B

General views of Fractures A and B in Specimen 6.

Figure 8.1. Figure 8.2 Figure 8.3

General views of Fractures A and B in Specimen 7.

Figure 9.1.

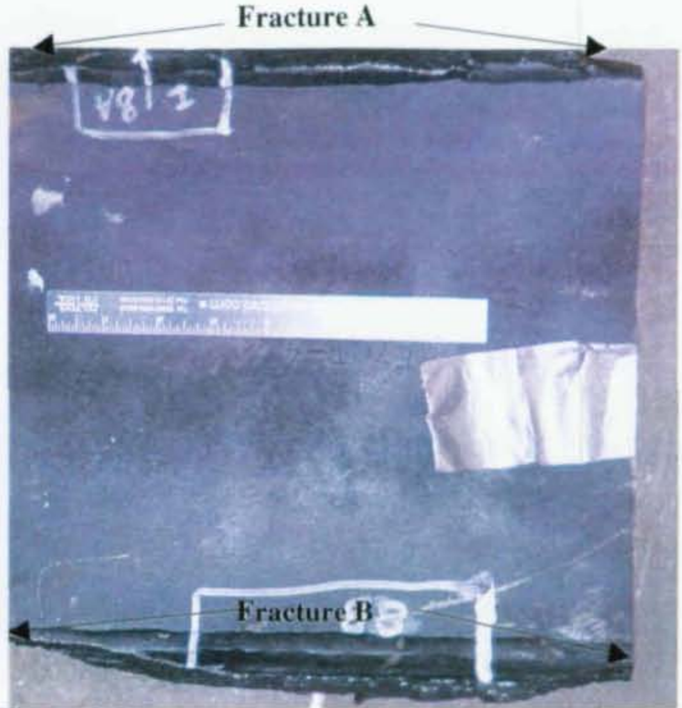

Figure 9.2.

Figure 9.3. Fracture 8A

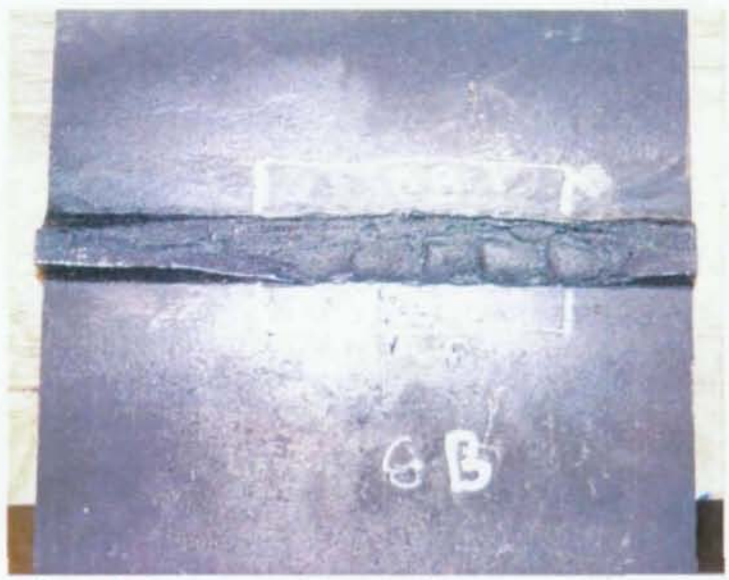

Figure 9.4. Fracture 8B

General views of Fractures A and B in Specimen 8.

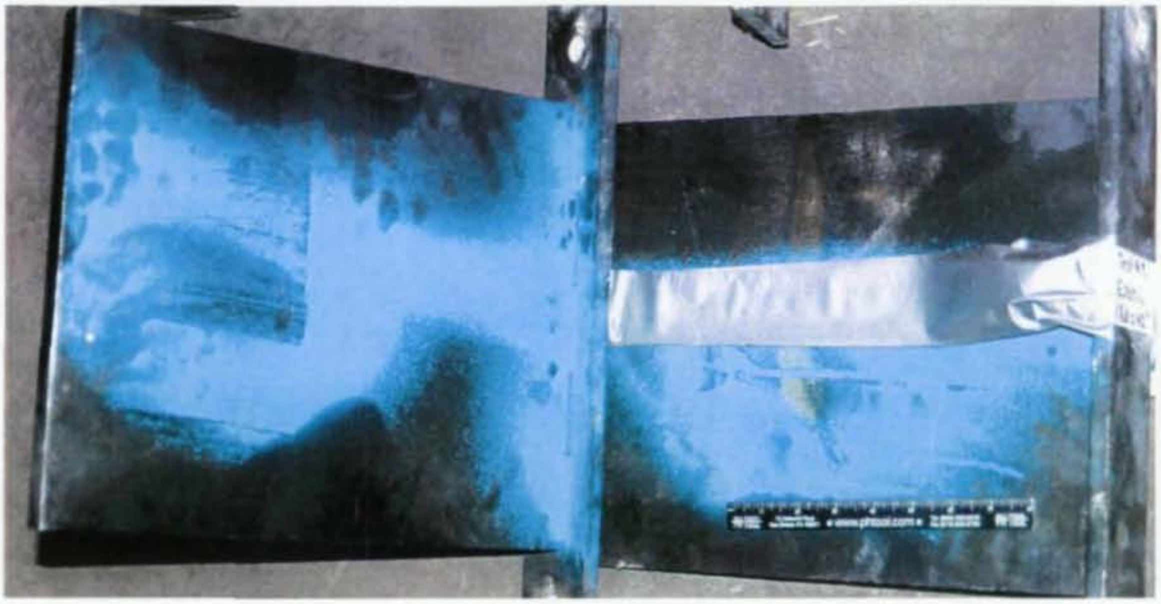

Figure 10.1.

Figure 10.2. Web side of fracture

Figure 10.3. Flange side of fracture

General views of fracture in Specimen 9.